ISSN 0255-7193

CLAY RESEARCH

Vol. 38, No. 1

June, 2019

IOS Press

Overseas distribution
IOS Press, The Netherlands

THE CLAY MINERALS SOCIETY OF INDIA
Division of Soil Science and
Agricultural Chemistry
Indian Agricultural Research Institute
New Delhi-110 012, India

Overseas subscribers may send
their queries to IOS Press, Nieuwe
Hemweg 6B, 1013 BG Amsterdam,
The Netherlands, orders@iospress.in:
URL: http://www.iospress.nl

THE CLAY MINERALS SOCIETY OF INDIA

(Registered under Act XXI of 1860)
Registration No. S/13028 of 1982

COUNCIL FOR 2019–20

President	:	Dr. S.C. Datta
Vice Presidents	:	Dr. Nayan Ahmed; Dr. P. Chandran
Secretary	:	Dr. S.K. Mahapatra
Joint Secretaries	:	Dr. Gautam Goswami; Dr. Saumitra Das
Treasurer	:	Ms. Ritu Nagdev
Chief Editor	:	Dr. Siddhartha S. Mukhopadhyay
Editors	:	Dr. K. M. Manjaiah; Dr. D.C. Nayak; Dr. S.K. Roy
		Dr. P. Chandran
Councilor	:	East Zone : Dr. Siladitya Bandyopadhyay, Dr. Prasenjit Roy
	:	West Zone : Dr. P. Chandran; Dr. D. Raja
	:	North Zone : Dr. U.K. Maurya, Dr. T. Satyanarayana
	:	South Zone : Dr. Anil Kumar K.S.
	:	Central Zone : Dr. Vassanda Coumar, Dr. Ranjan Paul
Past Presidents	:	Dr S.K. Mukherjee, Dr K.V. Raman, Dr S.K. Ghosh,
		Dr. D.K. Pal, Dr. Dipak Sarkar, Dr. Kunal Ghosh, Dr. S.K. Singh

INTERNATIONAL EDITORIAL CONSULTANT

International Consulting Editor	:	Dr. S.R. Krishnamurti Gummuluru Adjunct Associate Professor, CERAR, University of South Australia, Canada Dr. Sridhar Komarneni Adjunct Professor of Civil and Environmental Engineering & Editor-in-Chief, J. Porous Materials, USA

Annual Institutional Subscription Rates Inclusive of Air Mail and Handling Charges :

Subscription Rates (Year 2011)	Indian (INR)	Overseas (USD)
Print + online access	Rs. 1,800.00	$ 350.00
Online access	Rs. 600.00	$ 150.00
Print	Rs. 1,200.00	$ 200.00

All payments should be sent to **"The Clay Minerals Society of India"** Division of Soil Science and Agricultural Chemistry, I.A.R.I., New Delhi-110 012

Clay Research, Vol. 38, No. 1, pp. 1-11 (2019)

Metronidazole Drug Delivery: Theoretical Investigation of the Intercalation in the Interlayer Clay

R. DJEFAFLIA [1,2], D. LERARI [1], P. RAMASAMI [3,4], K. BACHARI [1]

[1]*Scientific and Technical Research Center in Physicochemical Analysis, BP 384, Bou-ismail industrial zone. RP 42004. Tipaza, Algeria*
[2]*Faculty of Science and Technology, Mohamed Cherif Messaadia University, B.P 1553 Souk-Ahras, Algeria*
[3]*Computational Chemistry Group, Department of Chemistry, Faculty of Science, University of Mauritius, Réduit 80837, Mauritius*
[4]*Department of Chemical Sciences, Faculty of Sciences, University of Johannesburg, Doornfontein, Johannesburg 2028, South Africa*

Abstract–This article presents a theoretical study of the interactions of the drug Metronidazole (Mt) intercalated in interlaminar Montmorillonite (MMT), where the geometry optimization was done by the Forcite module of the Materials studios 7.0 software, modifying the cations ($Ca2^{+}$, Mg^{2+}, Na^{+}, K^{+}, Fe^{3+}, Li^{+}) of MMT. The results obtained after the geometrical optimization of Mt in MMT are differentiated according to the type and nature of intercalation cations and the number of MMT layers. This article also shows that montmorillonite is a good way to test or improve the dissolution of the drug, but taking into account the nature, such as the type of cation used in montmorillonite and the number of layers of clay. According to our study, we can choose the best cation of clay that meets our interests and determines our strategy of working in the field of clays and drugs. The exothermic reactions are predicted by the interactions between the drug molecules and each cation and by the electrostatic force created between the layers.

Keywords: Electrostatic force; Montmorillonite; molecular simulation; intercalation in Montmorillonite; interlayer cation.

Metronidazole is an antibiotic drug used to treat different kinds of infections. It is available in oral, rectal, vaginal and topical preparations. Metronidazole is commonly used for vaginal infections for which pregnant women require treatment. It has been available in the market for more than 40 years. Metronidazole is also known as Flagy (Burtin, 1995). Due to its effectiveness, Metronidazole is considered as a prime drug for several pathologies (Lam *et al.,* 2001). The need for safe, therapeutically effective, and patient compliant drug delivery systems continuously leads researchers to design novel tools and strategies. Clay minerals play a very crucial role in modulating drug delivery (Joshi *et al.,* 2009). Clays are common ingredients in pharmaceutical products as both excipients and active substances. Clay minerals are naturally occurring inorganic cationic exchangers and so they may undergo ion exchange with basic drugs in solution. Smectites, especially, montmorillonite (MMT) and saponite, have been commonly studied because of their higher cation exchange capacity compared to other pharmaceutical silicates (such as talc, kaolin and fibrous clay minerals) (Aguzzi *et al.,* 2007). Clay minerals have continuously attracted attention for the possibility of modifying their layered structure by intercalation, thus creating new materials, such as adsorbents (Wu *et al.,* 2001), catalysts (Ji *et al.,* 2004), nanocomposite precursors (Maiti *et al.,* 2002) and materials with attractive electric or optical

***Corresponding Author Email :** samira.djefaflia@yahoo.com

properties (Chashechnikova *et al.,* 2005). Among possible layered solids, the smectite group of layered clay minerals (especially montmorillonite) provides attractive features, such as large surface areas, swelling behavior and ion exchange properties. Clay minerals are part of a family of layered materials, which have important environmental and engineering applications (Van Olphen, 1977; Teng, 1974; Bleam, 1993). Montmorillonite clay belong to the smectite group, and composed of silica tetrahedral sheets layered between alumina octahedral sheets. The imperfection of the crystal lattice and the isomorphous substitution induce a net negative charge that leads to the adsorption of alkaline earth metal ions in the interlayer space. Such imperfection is responsible for the activity and exchange reactions with organic compounds. Montmorillonite also contains dangling hydroxyl end groups on the surfaces (Kong *et al.,* 2010). It has large specific surface area and exhibits good adsorption ability, cation exchange capacity, standout adhesive ability, and drug-carrying capability. Thus, it is a common ingredient as both the excipient and active substance in pharmaceutical products (Khalil *et al.,* 2005). The intercalation of organic species into layered inorganic solids provides a useful and convenient route to prepare organic-inorganic hybrids that contain properties of both the inorganic host and organic guest in a single material (Wang *et al.,* 2008). In recent years, smectite clays intercalated by drug molecules have attracted great interest from researchers since they exhibit novel physical and chemical properties (Mohanambe *et al.,* 2005). Computer simulations have become an important tool to study the interfacial structures of clay materials. (Greenwell *et al.,* 2006) reviewed the use of computer simulations of clay minerals and pointed out that molecular simulation techniques can provide direct information on the swelling stability and interlayer structure of clay minerals (Whitley *et al.,* 2004; Karaborni *et al.,* 1996; Chavez-Paez *et al.,* 2001; Liu *et al.,* 2006; De Pablo *et al.,* 2005; Chavez *et al.,* 2004; Rutkai *et al.,* 2008). Recently, molecular modeling has been recognized as an efficient method for understanding the interlayer microstructure of clay minerals (Xi *et al.,* 2005; Bergaya *et al.,* 2006; He *et al.,* 2006; Lagaly, 1981; Vaia *et al.,* 1994; Othmani-Assmann *et al.,* 2007). A previous study (Wu *et al.,* 2015) was devoted to the influence of intercalated cations on the organic interaction of montmorillonite, where molecular simulation was carried out under the "CASTEP" module of Materials Studio 6.0 Software to study sorption sites of Na^{+}, K^{+}, Mg^{2+}, Ca^{2+} and Fe^{3+} on Montmorillonite. Based on the approach presented in (Wu *et al.,* 2015), the purpose of this paper was to study the interaction of Metronidazole (Mt) in the montmorillonite clay medium with exchange site cations.

Materials and Methods

We started by investigating the clay model MMT where its unite formula is $Al_2Si_4O_{10}(OH)_2Ca0.5$ in the lattice 3D triclinic. Montmorillonite with the interlayer cations Ca^{2+}, Mg^{2+}, Na^{+}, K^{+}, Fe^{3+}, Li^{+} are represented by Ca-MMT, Mg-MMT, Na-MMT, K-MMT, Fe-MMT and Li-MMT, respectively. Geometry optimization of all the prepared models was carried out in Materials Studio 7.0 software (Materials Studio. Accelrys Software Inc., San Diego., 2013) under the Forcite module (Accelrys Software Inc. 2012), using the Universal Force Field (Rappé *et al.,* 1992). This force field was previously used successfully for the modeling of organic compounds in the interlayer space of phyllosilicates (Klika *et al.,* 2004; Holešová *et al.,* 2009; Klika *et al.,* 2009). Materials Studio is now being used effectively over more than a decade for numerous different applications across a range of physical and chemical sciences and almost every industrial sector (Reinier *et al.,* 2015). Materials Studio Forcite is an advanced

classical molecular mechanics tool that allows fast energy calculations and reliable geometry optimization of molecules and periodic systems (Accelrys Software Inc. 2012). The Forcite simulation was performed on Metronidazole in the montmorillonite medium. The interactions between Mt and MMT medium and their cations were studied.

The crystallographic parameters for the single layer cell are α = 0.518 nm, b = 0.898 nm, c = 0.15 nm and $\alpha = \beta = \gamma = 90°$, but for the two layers cell are a = 0.518 nm, b = 0.898 nm, c = 2.922 nm and $\alpha = \beta = \gamma = 90°$. For the super cell, the parameters are a = 1.554 nm, b = 2.694 nm, c = 5.845 nm and $\alpha = \beta = \gamma = 90°$. In this study, we created super cell (3×3×4). Before starting the optimization, the distances between the reference atom of MMT (R.MMT) and the nitrogen atom of Metronidazole (N.Mt), and the left cation and the right cation of interlayer space of montmorillonite were calculated. The values of these distances are R.MMT and N.Mt = 0.256 nm, R.MMT and left cation = 0.492 nm, R.MMT and cation right = 0.624 nm (Figs. 1, and 2).

Based on the selected cation, the values of theses parameters were modified (case of a single layer and between two layers), as listed in (Table 1). Fig. 3 illustrates the geometries obtained.

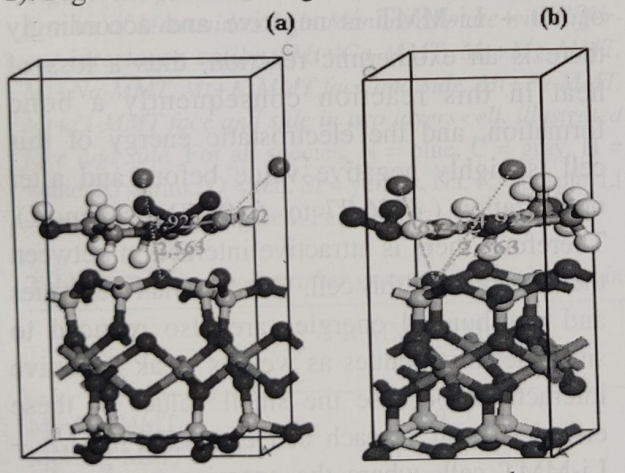

Fig. 1. *Calculation of the distances between the atoms selected and the reference mark of MMT. (State initial before optimization in the single layer cell), face (1a) and side (1b).*

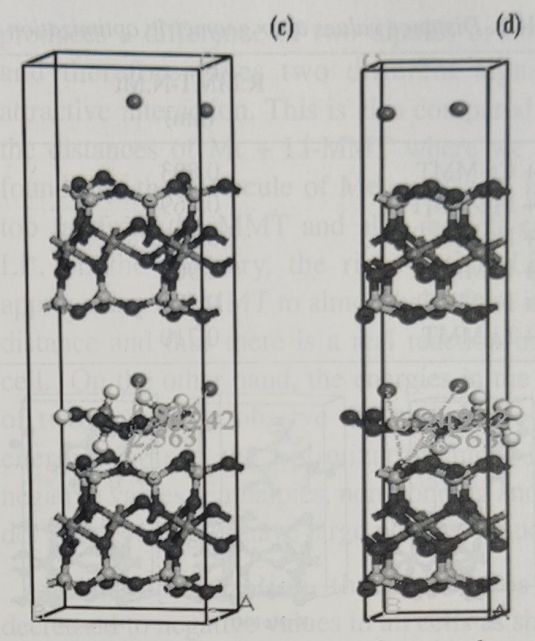

Fig. 2. *Calculation of the distances between the atoms selected and the reference mark of MMT. (State initial before optimization in the two-layer cell), face (2c) and side (2d).*

Results and Discussion

The results indicate that the distances between the selected atoms increase compared to the initial state (before optimization). The molecule of Metronidazole is a little distant from Fe-MMT and it is far from Mg-MMT and Na-MMT, on the other hand it is very far from Li-MMT, Ca-MMT and K-MMT where Metronidazole is partially removed from the cell of MMT.

Even the distances between the cations and the Montmorillonite are increased, such that the cations are far from MMT except the right cation Ca^{2+} and cation right Fe^{3+} and cation left K^{+} are not very far. However, the right cation Li^{+} is close to the MMT almost half the distance, and the left cation Fe^{3+} is far from MMT almost three times the initial distance. There is a different repulsion depending on the nature of the cation. (Fig. 4) represents the face and side geometries of the different cells of MMT (two layers) with its cation and the molecule of Metronidazole. As

Table 1. *Distance values after geometric optimization in the case of a single layer.*

	R.MMT-N.Mt (nm)	R.MMT-left cation (nm)	R.MMT-right cation (nm)
Mt + Ca-MMT	0.893	0.891	0.642
Mt + Mg-MMT	0.669	0.870	0.893
Mt + Na-MMT	0.600	0.869	0.814
Mt + K-MMT	0.906	0.540	0.852
Mt + Fe-MMT	0.584	1.214	0.693
Mt + Li-MMT	0.710	0.891	0.351

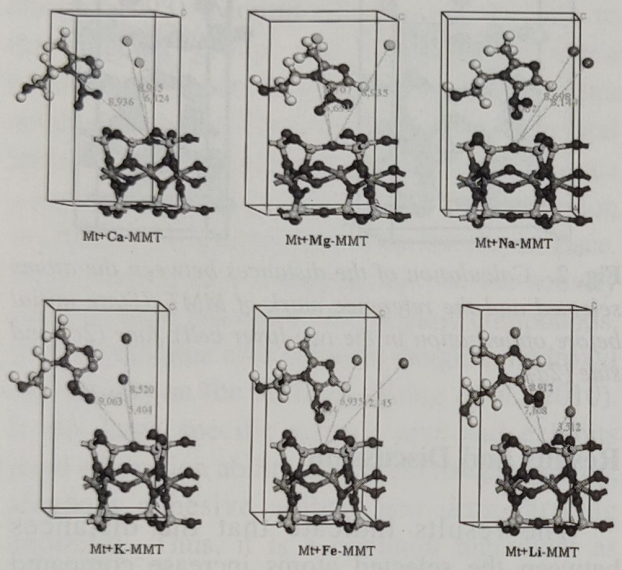

Fig. 3. *Geometrical optimization by the module of Forcite of Metronidazole in Montmorillonite with different interlayer cations, Mt+Ca-MMT, Mt+Mg-MMT, Mt+Na-MMT, Mt+K-MMT, Mt+Fe-MMT, Mt+Li-MMT in the single layer cell.* For all species, N, C = gray, H = white, Al = pink, O=red, Si = yellow, Na, K = purple, Li = mauve, Mg, Ca = green, Fe = violet.

shown in (Table 2), the distances values are large after the optimization. However, the molecule of Metronidazole (Mt) is removed slightly from the MMT and partially removed from the cell of Ca-MMT, Mg-MMT and Na-MMT. It came out of the square from the cell of K-MMT, Fe-MMT and Li-MMT. All the cations are away from the MMT and exit from the cell except that the left cation Na^+ is very close to the MMT, and the right cation Mg^{2+} is a little distance away and remained in the cell. We note that the molecule of MMT move away from the cell, except in the Mt+Na-MMT and Mt+Mg-MMT where it stays in the cell. On the energetic side, the results obtained agree to each other of each cell of the different cations of a single layer or two layers.

The energy outcomes are grouped in the following tables (Tables.3-6) and this is followed by their graphical representations (Figs.5-8).

We observe that the total enthalpies are the total energies and they have very large positive values. The non-bonded energies and van der Waals against the electrostatic energies are zero in all cells except Mt + Li-MMT, which has a large negative value. After optimization almost all energy values are reduced, but the values of enthalpies, non-bonded energies and van der Waal's are reduced from very large to small values. The values of the enthalpies after the optimization are positive except for the enthalpy of Mt + Li-MMT, which is negative. The enthalpy of Mt + Li-MMT is negative and accordingly there is an exothermic reaction, thus a loss of heat in this reaction consequently a bond formation, and the electrostatic energy of this cell is highly negative value before and after optimization (-3186.77 to -3498.71 kcal mol^{-1}), Therefore, there is attractive interaction between the molecules of this cell. Van der Waal's energies and non-bonded energies are also reduced to small negative values as well as weak attractive interactions because the small values of these energies occur in each cell except in the Mt + Li-MMT cell, where the energies non-bonding and van der Waals have larger values.

These led us to explain that the cation of Li^+ is responsible for large polarizability. This

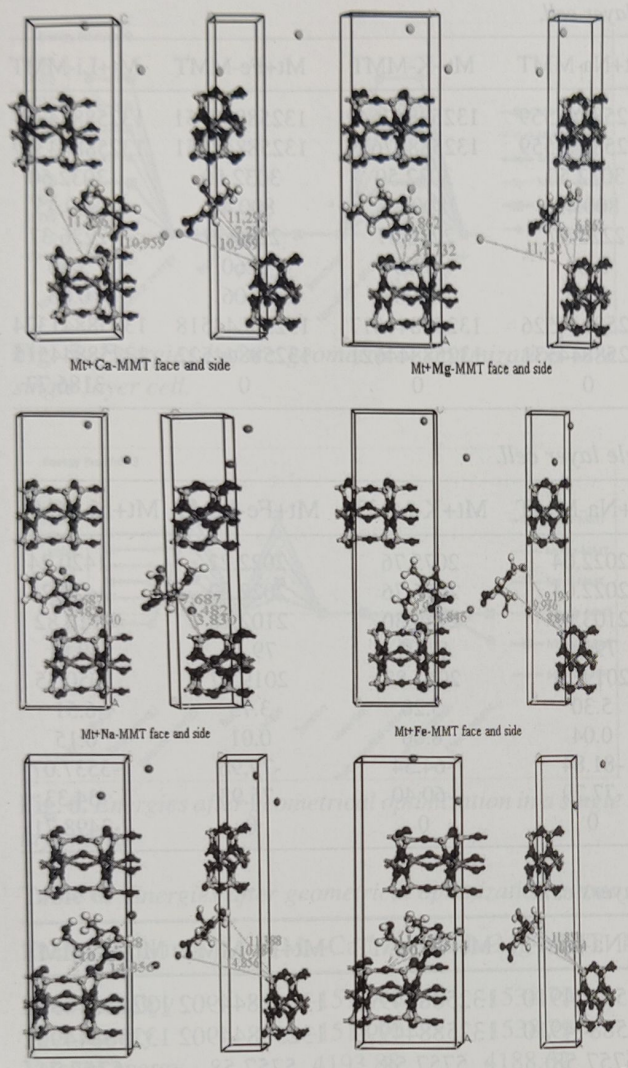

Fig. 4. *All geometrical optimizations by the module of Forcite of Metronidazole in Montmorillonite with different interlayer cations Mt+Ca-MMT, Mt+Mg-MMT, Mt+Na-MMT, Mt+K-MMT face and side, Mt+Fe-MMT, Mt+Li-MMT face and side in two layers cell, illustrated face and side.* For all species, N = blue, C = gray, H = white, Al = pink, O = red, Si = yellow, Na, K = purple, Li = mauve, Mg, Ca = green, Fe = violet.

produces a difference of two dipoles or charges and therefore gives two different signs for attractive interaction. This is also compared with the distances of Mt + Li-MMT where we have found that the molecule of Metronidazole is not too far from the MMT and also the left cation Li^+, on the contrary, the right cation Li^+, is approaching the MMT to almost half of the initial distance and thus there is a real reaction in this cell. On the other hand, the energies in the case of two layers, we observe that the electrostatic energies before the optimization have large negative values. Enthalpies, non-bonding and van der Waal's energies have large positive values.

After optimization the enthalpies are decreased to negative values in all cells as shown in (Fig. 3 and 4) and the values are as follows: Mt + Ca-MMT (-1511.90 kcal mol^{-1}), Mt + Mg-MMT (-1538.79 kcal mol^{-1}), Mt + Na-MMT (-1519.37 kcal mol^{-1}), Mt + K-MMT (-1503.24 kcal mol^{-1}), Mt + Fe-MMT (-1546.44 kcal mol^{-1}), Mt + Li-MMT (- 1530.13 kcal mol^{-1}). We can deduce that the number of layers influences on the reactions between the layers, because before the optimization we have found that the electrostatic energies are not zero so there are interactions between the molecules, and after the optimization enthalpies are decreased to small negative values, so there is an exothermic reaction in every cell of two layers.

The non-bonded and van der Waals energies are decreased but they are large negative values, so there are attractive interactions in the cells of each cation. We conclude that the reaction from

Table 2. *Distance values after geometric optimization in the case of a two layers cell.*

	R.MMT-N.Mt (nm)	R.MMT-left cation (nm)	R.MMT-right cation (nm)
Mt+**Ca**-MMT	0.729	1.129	1.095
Mt+**Mg**-MMT	0.552	0.686	1.173
Mt+**Na**-MMT	0.548	0.768	0.383
Mt+**K**-MMT	1.048	1.138	1.485
Mt+**Fe**-MMT	0.993	0.919	0.884
Mt+**Li**-MMT	1.050	1.185	1.151

Table 3. *All energies before geometrical optimization in a single layer cell.*

Energy (kcal mol^{-1})	Mt+Ca-MMT	Mt+Mg-MMT	Mt+Na-MMT	Mt+K-MMT	Mt+Fe-MMT	Mt+Li-MMT
Total enthalpy	13258847671	13258847579	13258847559	13258847649	13258847551	13258844357
Total energy	13258847671	13258847579	13258847559	13258847649	13258847551	13258844357
Valence energy	3032.50	3032.50	3032.50	3032.50	3032.50	3032.50
Bond	800.45	800.45	800.45	800.45	800.45	800.45
Angle	2226.37	2226.37	2226.37	2226.37	2226.37	2226.37
Torsion	5.60	5.60	5.60	5.60	5.60	5.60
Inversion	0.06	0.06	0.06	0.06	0.06	0.06
Non-bonded energy	13258844639	13258844547	13258844526	13258844617	13258844518	13258841324
van der Waals	13258844643	13258844551	13258844531	13258844621	13258844522	13258844515
Electrostatic	0	0	0	0	0	-3186.77

Table 4. *All energies after geometrical optimization in single layer cell.*

Energy (kcal mol^{-1})	Mt+Ca-MMT	Mt+Mg-MMT	Mt+Na-MMT	Mt+K-MMT	Mt+Fe-MMT	Mt+Li-MMT
Total enthalpy	2064.36	2025.25	2022.04	2075.76	2022.22	-1420.24
Total energy	2064.36	2025.25	2022.04	2075.76	2022.22	-1420.24
Valence energy	2140.09	2102.67	2103.88	2140.30	2102.18	2116.82
Bond	81.61	77.94	79.40	81.21	79.14	59.81
Angle	2044.92	2020.02	2019.13	2045.82	2019.27	2050.35
Torsion	5.54	4.67	5.30	5.20	3.75	6.51
Inversion	8.01	0.03	0.04	8.06	0.01	0.15
Non-bonded energy	-75.73	-77.41	-81.84	-64.54	-79.96	-3537.07
van der Waals	-71.47	-73.30	-77.79	-60.40	-75.93	-34.33
Electrostatic	0	0	0	0	0	-3498.71

Table 5. *Energies before geometrical optimization in two layers cell.*

Energy (kcal mol^{-1})	Mt+Ca-MMT	Mt+Mg-MMT	Mt+Na-MMT	Mt+K-MMT	Mt+Fe-MMT	Mt+Li-MMT
Total enthalpy	13258845019	13258844929	13258844910	13258844999	13258844902	13258844922
Total energy	13258845019	13258844929	13258844910	13258844999	13258844902	13258844922
Valence energy	5757.58	5757.58	5757.58	5757.58	5757.58	5757.71
Bond	1321.87	1321.87	1321.87	1321.87	1321.87	1321.88
Angle	4422.62	4422.62	4422.62	4422.62	4422.62	4422.61
Torsion	10.48	10.48	10.48	10.48	10.48	10.61
Inversion	2.60	2.60	2.60	2.60	2.60	2.60
Non-bonded energy	13258839261	13258839171	13258839152	13258839242	13258839145	13258839164
van der Waals	13258844564	13258844474	13258844455	13258844544	13258844447	13258844442
Electrostatic	-5295.98	-5295.98	-5295.98	-5295.98	-5295.98	-5271.41

MT with the MT depends of number of the layers and nature of cation. We chose Na^+ to study the super cell of Mt + Na-MMT. (Fig. 9) represents the supercell Mt + Na-MMT before optimization and table 7 summarizes the distances before and after the optimization of Mt + Na-CMM super cell.

We observed that before optimization, the Metronidazole molecules were introduced in a flat and horizontal position and in parallel with the Montmorillonite, and even the cations were classified in parallel in lines (Fig. 9), but after the optimization the molecules of the Metronidazole Mt became perpendicular to Montmorillonite, and the cations did not remain in lines but they did a zigzag form as shown in (Fig.10). The results of the energies are collected in (Table 8).

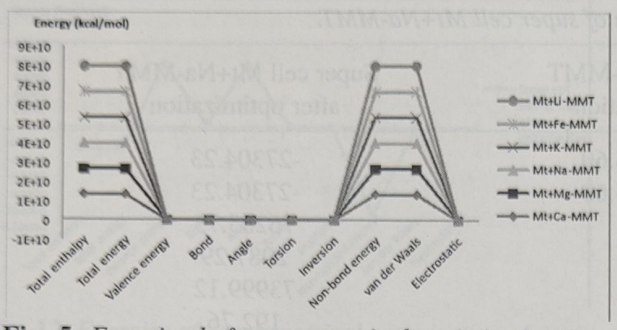

Fig. 5. *Energies before geometrical optimization in a single layer cell.*

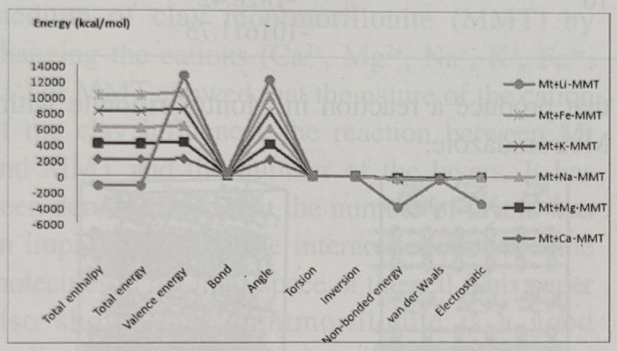

Fig. 6. *Energies after geometrical optimization in a single layer cell.*

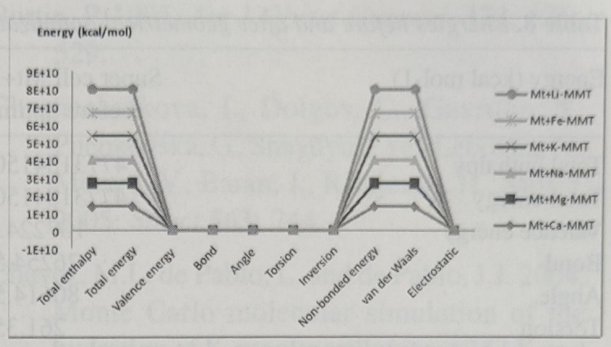

Fig. 7. *All energies before geometrical optimization in two layers cell.*

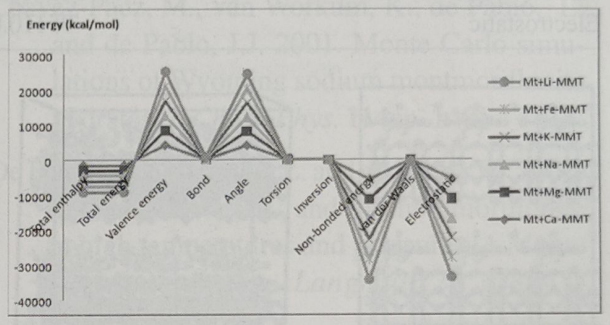

Fig. 8. *All energies after geometrical optimization in two layers cell.*

Table 6. *Energies after geometrical optimization in two layers cell.*

Energy (kcal mol^{-1})	Mt+Ca-MMT	Mt+Mg-MMT	Mt+Na-MMT	Mt+K-MMT	Mt+Fe-MMT	Mt+Li-MMT
Total enthalpy	-1511.90	-1538.79	-1519.37	-1503.24	-1546.44	-1530.13
Total energy	-1511.90	-1538.79	-1519.37	-1503.24	-1546.44	-1530.13
Valence energy	4193.88	4188.62	4190.68	4197.32	4188.72	4192.64
Bond	117.04	116.22	115.26	117.47	115.80	115.58
Angle	4066.20	4061.77	4060.10	4068.52	4060.52	4066.47
Torsion	9.90	10.45	14.60	10.19	11.94	10.13
Inversion	0.73	0.16	0.70	1.13	0.45	0.44
Non-bonded energy	-5705.78	-5727.42	-5710.05	-5700.57	-5735.16	-5722.77
van der Waals	-104.49	-101.00	-99.60	-96.76	-93.73	-92.34
Electrostatic	-5594.14	-5619.53	-5603.68	-5596.89	-5634.71	-5623.72

Table 7. *Distance before and after geometric optimization in the super cells of Mt+Na-MMT.*

Distance between atoms (D) (Å)	Before	After
R.MMT and N.Mt	0.498	0.723
R.MMT and left cation Na^+	0.517	0.695
R.MMT and right cation Na^+	0.624	0.874

We observed that the distances between atoms are large after optimization. The positions of the molecules and the atoms changed and removed but these are well organized and well determined in the super-cell. The results of all energies before and after geometrical optimization of supercell Mt+Na-MMT are displayed in (Fig. 11 and 12).

The energies, given in the (Table 8), of supercell Mt + Na-MMT, indicate that enthalpy or total energy and also non-bonded energy and van der Waal's have large positive values before optimization compared to other energies, and the

Table 8. *Energies before and after geometrical optimization of super cell Mt+Na-MMT.*

Energy (kcal mol-1)	Super cell Mt+Na-MMT before optimization	Super cell Mt+Na-MMT after optimization
Total enthalpy	477318415023.60	-27304.23
Total energy	477318415023.60	-27304.23
Valence energy	107224.33	76285.75
Bond	26254.56	2087.29
Angle	80614.51	73999.12
Torsion	261.35	192.76
Inversion	93.89	6.57
Non-bonded energy	477318307799.26	-103589.98
van der Waals	477318403059.10	-1828.42
Electrostatic	-95110.03	-101611.75

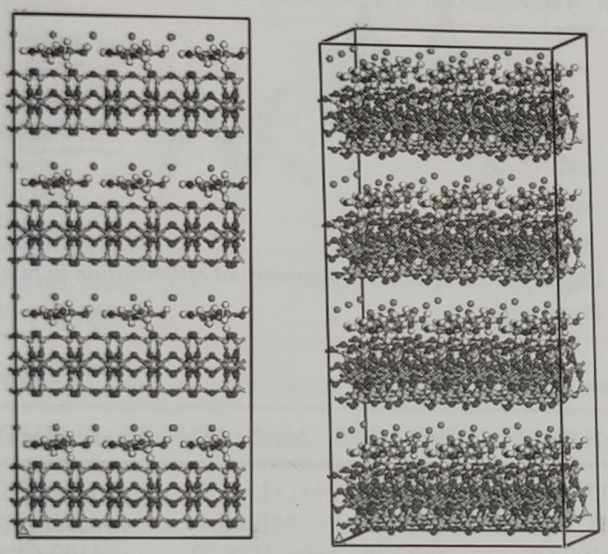

Fig. 9. *The super cells of Mt+Na-MMT before optimization face and side.*

electrostatic energy has a large negative value, and after optimization, the energies are decreased, but the total enthalpy is decreased to -27304.23kcal mol-1 a large negative value, so the reaction is exothermic, and the non-bonded and van der Waals energies are decreased to negative values. We also observed that the electrostatic energy is negative and is greatly diminished to -101611.75 kcal mol-1, and the electrostatic energy of a system of charges, initially supposed to be far from each other, corresponds to the work required provide to bring these charges to their final positions. Therefore, there are attractive interactions in the super cell that produce a reaction in Montmorillonite with Metronidazole.

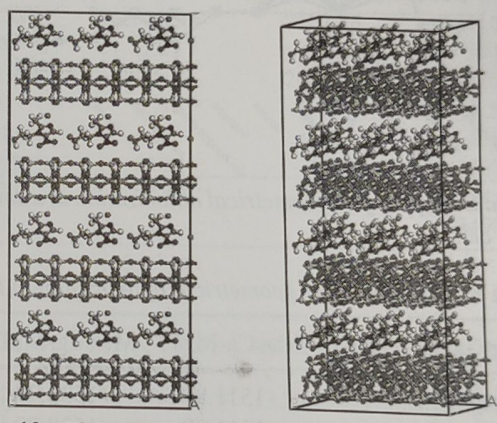

Fig. 10. *The super cells of Mt+Na-MMT after optimization face and side.*

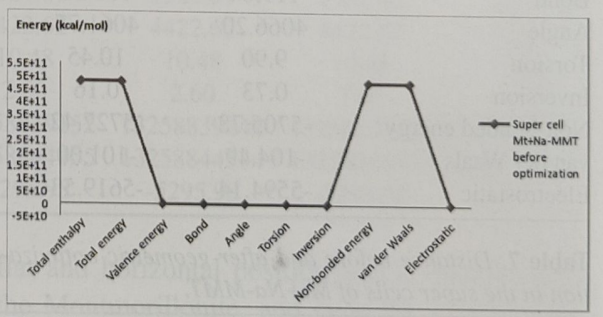

Fig. 11. *Energies before geometrical optimization of super cell Mt+Na-MMT.*

Conclusion

The geometry optimization with the module of Forcite of the software Materials studio 7.0, on the molecule of Metronidazole (Mt) in the

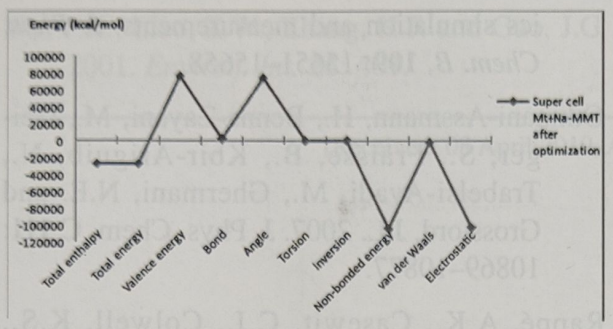

Fig. 12. *Energies after geometrical optimization of super cell Mt+Na-MMT.*

medium of clay montmorillonite (MMT) by changing the cations (Ca^{2+}, Mg^{2+}, Na^{+}, K^{+}, Fe^{3+}, Li^{+}) of MMT showed that the nature of the cation of the clay influences the reaction between Mt and MMT and the number of the layers. It has been demonstrated that the number of layers was an impact factor on the interactions between the molecules in the inter-space of the cell. This paper also shows that montmorillonite is a good medium for testing or improving the dissolution of the drug but taking in the account the nature, such as the type of cation used in montmorillonite and the number of clay layers. According to our study, we can choose the best cation in the clay that meets our interests and determines our working strategy in the field of clays and drugs.

References

Accelrys Software Inc. 2012: Forcite program. *San Diego, CA*.

Aguzzi, C., Cerezo, P., Viseras, C., Caramella, C. 2007. Use of clays as drug delivery systems:Possibilities and limitations. *Applied Clay Sci.*. **36**: 22–36

Bergaya, F., Theng, B.K.G., Lagaly, G. 2006., *Develop. Clay Sci.* **1**: 499.

Bleam, W.F. 1993. Atomic theories of phyllosilicates: Quantum chemistry, statistical mechanics, electrostatic theory, and crystal chemistry, *Rev. Geophys.* **31**: 51 – 73.

Burtin, P. 1995. *Am J Obstet Gynecol.* **172**, 525 - 529.

Chashechnikova, I., Dolgov, L., Gavrilko, T., Puchkovska, G., Shaydyuk, Ye., Lebovka, N., Moraru, V., Baran, J., Ratajczak, H., Mol, J. 2005. *Struct.***563**: 744

Chavez, M.L. de Pablo, L. and de Pablo, J.J. 2004. Monte Carlo molecular simulation of the hydration of K-montmorillonite at 353 K and 625 bar, Langmuir 20: p. 10764 – 10770.

Chavez-Paez, M., van Workum, K., de Pablo, L. and de Pablo, J.J. 2001. Monte Carlo simulations of Wyoming sodium montmorillonite hydrates, *J. Chem. Phys.* **114**: p. 1405 – 1413.

De Pablo, L., Chavez, M.L. and de Pablo, J.J. 2005. Stability of Na-, K-, and Ca-montmorillonite at high temperatures and pressures: A Monte Carlo simulation. *Langmuir* ***21***:10874 – 10884.

Greenwell, H.C., Jones, W., Coveney, P.V. and Stackhouse, S. 2006. On the application of computer simulation techniques to anionic and cationic clays: A materials chemistry perspective. *J. Mater. Chem.* **16**: 708–723.

He, H.P., Duchet, J., Galy, J., Gérard, J.F. 2006. *J. Colloid Interf. Sci.* **295**:202–208.

Holešová, S., Kulhánková, L., Simha Martynková, G., Kukutschová, J., Èapková, P. 2009. An effective route to montmorillonite intercalation with imidazole complexes: Experiment and theory. *J. Molecular Structures.* **923** (1-3): 85-89.

Ji, J.-Q., Black, L., Weidler, P.G., Janek, M. 2004. *Langmuir* **20**: 9796.

Joshi, G. V., Kevadiya, B. D., Patel, H. A., Bajaj, H. C and Jasra, R. V. 2009. Montmorillonite as a drug delivery system: intercalation and in vitro release of timolol maleate. *Inter. J. Pharmaceutics.* **374**(1-2):53–57.

Karaborni, S., Smit, B., Heidug, W., Urai, J. and van Oort, E. 1996. The swelling of clays:

Molecular simulations of the hydration of montmorillonite, Science **271**: 1102 – 1104.

Khalil, H., Mahajan, D. and Rafailovich, M. 2005. Polymer-montmorillonite clay nanocomposites. Part 1: complexation of montmorillonite clay with a vinyl monomer. *Polymer Intern.* **54**:423-427.

Klika, Z., Pustková, P., Praus, P., Kováø, P., Pospíšil, M., Malý, P., Grygar, T., Kulhánková, L.,Èapková, P. 2009. Fluorescence of reduced charge montmorillonite complexes with methylene blue: Experiments and molecular modeling. *J. Colloid Interface Sci.* **339**:416-423.

Klika, Z., Weissmannová, H., Èapková, P., Pospíšil, M. 2004. The rhodamine B intercalation of montmorillonite. *J. Colloid Interface Sci.* **275**: 243-250.

Kong, M., Chen, X. G., Xing, K., Park, H. J. 2010. Antimicrobial properties of chitosan and mode of action: a state of the art review. *Intern. J. Food Microb.* **144**:51–63.

Lagaly, G. 1981. *Clay Miner.* **16**: 1–21.

Lam, A., Rivera, A., Fuentes, G.R. 2001. *Microporous Mesoporous Mater.* **49**: 157-162.

Liu, X.D. and Lu, X.C. 2006. A thermodynamic understanding of clay-swelling inhibition by potassium ions, Angew. *Chem. Int. Ed.* 45: p. 6300– 6303.

Maiti, P., Yamada, K., Okamoto, M., Ueda, K., Okamoto, K. 2002. *Chem. Mater.* **14**: 4654.

Materials Studio. Accelrys Software Inc., San Diego. Note that some of these codes were also offered as part of the Cerius 2 application that preceded Materials Studio; 2013. Available from http://accelrys.com/products/materials-studio/

Mohanambe, L., Vasudevan, S. 2005. Anionic clays containing anti-inflammatory drug molecules: comparison of molecular dynamics simulation and measurements. *J. Phys. Chem. B*, **109**: 15651–15658.

Othmani-Assmann, H., Benna-Zayani, M., Geiger, S., Fraisse, B., Kbir-Ariguib, N., Trabelsi-Ayadi, M., Ghermani, N.E. and Grossiord, J.L. 2007. J. Phys. Chem. C **111**: 10869–10877.

Rappé, A.K., Casewit, C.J., Colwell, K.S., Goddard III, W.A. and Skiff, W.M. Uff. 1992. A full periodic table force field for molecular mechanics and molecular dynamics simulation. *J. Amer. Chemical Soc.* **114 (25):** 10024-10035.

Reinier L.C. Akkermans, Neil A. Spenley and Struan H. Robertson, 2015. Monte Carlo methods in Materials Studio. *Molecular Simulation.* **39**(14-15): 1153-1164.

Rutkai, G. and Kristof, T. 2008. Molecular simulation study of intercalation of small molecules in kaolinite. *Chem. Phys. Lett.* **462** : 269 – 274.

Teng, B.K.G. 1974. *The Chemistry of Clay-Organic Reactions*, Wiley, New York.

Vaia, R.A., Teukolsky, R.K., Giannelis, E.P. 1994. *Chem. Mater.* **6 (7)**: 1017–1022.

Van Olphen, H. 1977. *Clay Colloid Chemistry*, Wiley, New York.

Wang, X., Du, Y. and Luo, J. 2008. Biopolymer/montmorillonite nanocomposite: preparation, drug-controlled release property and cytotoxicity. *Nanotechnology.* **19**(6): Article ID 065707.

Whitley, H.D. and Smith, D.E. 2004. Free energy, energy, and entropy of swelling in Cs-, Na-, and Sr-montmorillonite clays. *J. Chem. Phys.* **120**: 5387–5395.

Wu, L., Liao, L. and Lv, G. 2015. Influence of interlayer cations on organic intercalation of montmorillonite. *J. Colloid Interface Sci.* **454**: 1-7.

Wu, P.X., Liao, Z.W., Zhang, H.F. and Guo, J.G. 2001. *Environ. Int.* **26**: 401.

Xi, Y.F., Frost. R.L., He, H.P., Kloprogge, T. and Bostrom, T. 2005. *Langmuir.* **21**: 8675-8680.

(Received: 08 April 2019, Accepted: 20 September 2019)

Clay Research, Vol. 38, No. 1, pp. 12-18 (2019)

Fabricating Copper-Based Composite by using Waste Steel Chips and TiB_2 Reinforcement Material

SHASHI PRAKASH DWIVEDI *, MAHESH PANDEY, PRADEEP YADAV, MD. SHAHNAWAZ, ARPIT SINGH AND JAYPEE YADAV

G. L. Bajaj Institute of Technology & Management, Greater Noida, Gautam Buddha Nagar, U.P., India

Abstract–*Nowadays the wastes of the steel from the manufacturing sectors are producing in very large quantity. However, industries are not able to reutilise these wastes as it is not fruitful for these industries. Therefore, In the present study, an attempt was made to developed copper-based composite material reinforced with waste steel chips and TiB_2 (Titanium diboride). Uniform distribution of reinforcement particles was observed in the copper-based matrix material. Mechanical properties such as hardness and tensile strength were improved by utilizing 5 wt. % waste steel chips and 5 wt. % TiB_2 in copper-based matrix. Tensile strength for Cu/5 wt. % steel chips composite and Cu/5 wt. % TiB_2 composite was found to be 220 MPa and 215 MPa respectively. Hardness was found to be 35 BHN and 45 BHN for Cu/5 wt. % steel chips composite and Cu/5 wt. % TiB_2 composite respectively.*

Key words*:* Copper, waste steel chips, reutilize, composite; TiB_2

Copper is denoted by Cu and it is a chemical element. It is ductile, higher electrical conductive and plentiful metal with useful properties. It has high corrosion resistance and easily joined (Alaneme, 2016). Now copper is also used to manufacture jewellery and ornament and also used as winding for motor, radio and TV sets. However, it was observed that the mechanical properties of copper are comparatively low as compared to steel. Steel manufacturing industries produced lots of waste scrap (Pavlovic, 2011). These scraps can be reused in various sectors. Steel is an alloy of iron and carbon and some other elements. It is composed of iron (Fe) with the little amount of carbon. Unalloyed steel contains from 0.002% to 2.1 % carbon. It is used in the modern construction, automobile machine, and weapon, building, needles and electronics. There are different types of Steel eg. carbon steel, alloy steel, stainless steel and tool steel. Steel is lighter than wood. Reinforcement is the action or process of reinforcing or strengthening (Nadoushani, 2015). It refers to an amplify its behaviour, but this term is also sometimes used to denote an amplification of memory. Strengthening effect may be measured as a higher frequency of the behaviour. Positive reinforcement provides a desirable stimulus. The stimulus is associated with wanting and liking. There is also negative reinforcement, which is characterized by taking away an undesirable stimulus (Du, 2009; Sapate, 2008). Table 1 showed a summary of copper-based composite with outcome results.

Pollution from the industry and agricultural waste is one of the most serious issues all over the world (Nagdev, 2018). Recycling or reuse of by-products (waste) is a goal to be achieved under the current economic and ecological crisis. The reuse of waste leads to saving energy and raw materials reduce environmental pollution and risk factors for public health and so on. The solid organic or inorganic wastes have been used as

***Corresponding Author Email :** spdglb@gmail.com

Table 1. *Copper-based composite materials and their utilities*

Author's Name	Material Used	Results Outcome and Conclusions
(Pavlovic, 2011)	Copper	Resistance level of reinforced concrete composite was examined.
(Bingcheng, 2015)	Copper matrix	The polymers were used for the replacement of fine aggregates with copper
(Du, 2009)	Textile-reinforced concrete	The flexural property of the BTRC was increased.
(Sapate, 2008)	SiC particles	The initially proposed general utilised method was employed for single phase Cu.
(Burri, 2014)	Carbon fiber reinforced plastics	In the absence of the baking the v properties produces the carbon fibre.
(Liang, 2019)	Copper/TiB whiskers and Copper/TiB_2 particles composite	Casting defects reinforcement clusters and shrinkage porosities that formed during the end stage of solidification were eliminated.
(Cho, 2019)	Copper-diamond composite materials	Particle size in electrodeposited composite materials strongly affect the microstructure of the metal matrix
(Gladkovsky, 2019)	Sandwich copper/steel composites	Sandwich composites have higher strength properties as compared to initial copper in 1.8–3.5 times
(Kavaliauskas, 2019)	Graphite-copper composites	Increase of copper content in initial powder from 2 to 60%, the microhardness of graphite copper composite coatings is reduced by about 2 times, while the plasticity increase from 11 to 19% is observed
(Afifeh, 2019)	Nanostructured copper matrix composite	The yield strength, ultimate tensile strength, and hardness of the 96% deformed copper matrix composite increased
(Gorbatyuk, 2019)	Copper-Molybdenum Composite	The introduction of the additional operations in the Mo-Cu composite technology process improve characteristics of the produced materials, and to increase the yield up to 85%
(Nazeer, 2019)	Copper-graphite composites	Graphite and graphene oxide mesh size (3500μm) gave good results compared with mesh sizes 500 μm and 1000 μm
(Zhang, 2019)	Graphene/copper composite	The yield strength (380 ±5 MPa) and tensile strength (412/±7 MPa) of 1.5/vol % graphene/copper composite were 74% and 30% higher than that of pure Cu
(Zhou, 2019)	Cu-Al_2O_3-Ag composite	The annealing treatment has insignificant impacts on EC of Cu Al_2O_3 without Ag
(Liu,Q. 2019)	Diamond/copper composites with Mo_2C in-situ nano-coating	The relative density and thermal conductivity increased with the thickening of Mo_2C coatings, while the coefficient of thermal expansion decreased with the thickening of Mo_2C coatings.
(Liu, R. 2019)	Graphite/copper composites	Large size graphite flake is the most promising heat dissipation fillers for Cu matrix composites, due to the high TC in two-dimensional plane and the good orientation in matrix
(Thankachana, 2019)	Cu/(25% AlN + 75% BN) composite	Results demonstrated an increase in mechanical properties with respect to increase in the amount of particle dispersion
(Chen, 2019)	Diamond/Copper composites	Understanding the thermal conductivity of Diamond/Copper composites by first-principles calculations
(Dong, 2019)	W-Cu composites	This critical review presents and discusses the current progress of W-Cu composites
(He, 2018)	Copper matrix composites reinforced by graphene nanosheets	The tribological performances were improved dramatically with increase of graphene nanosheets content
(Wang, 2019)	Graphene/copper composites	The addition of graphene increased the thermal and electrical conductivities, tensile and yield strengths, and hardness of the composites, but led to defect formation in the graphene due to the thermal expansion mismatch between graphene and copper

reinforcement material in the development of composite. All obtained composites present very good physical-mechanical properties: high hardness, good strengths at abrasion and the compressive strengths. They also have good thermal stability at high-temperature variation and high stability in different aggressive media (Ropota, 2013). Table 2 shows various waste materials used in the development of composite material.

It is observed from the literature review that very few researchers developed copper-based composite material using waste steel chips reinforcement material. However, (Alaneme, 2016) developed Cu/steel chips composite material and observed mechanical properties. But, they did not compare its property from copper/TiB_2 composite material. Keeping these facts in mind, in the present investigation, an attempt was made to utilize the waste steel chips in the development of copper-based composite material as reinforcement. Comparative study of waste steel chips as reinforcement in copper with TiB_2 was also carried out to observe the waste steel chips addition in the copper matrix material.

Materials and Methods

Copper-based composite materials reinforced with various ceramic particles and industrial waste can be developed by various casting techniques. In this study, the copper-based composite material was developed using stir casting technique. Stir casting technique is one of the simplest techniques to develop the metal matrix composite. Copper matrix materials were melted in muffle furnace inside the crucible. Ball milled waste steel chips as reinforcement material was added in melt matrix material as shown in Figure 1. Figure 2 shows the schematic diagram of Cu/TiB_2 composite development. The obtained microstructure of Cu/5 wt. % waste steel chips and Cu/TiB_2 composite were showed uniform distribution.

Results and Discussion

Development of aluminium based composite material by using various ceramic reinforcement materials and its characterization was one of the most common trends in material science engineering. Nowadays, copper is used in various

Table 2. *Waste material as reinforcement material in the development of composite*

Author's Name	Waste Reinforcement	Composite	Properties Examined
(Saurabh, 2015)	Urea	Nanoclay Polymer Composites (NCPCs) Loaded with Urea	XRD, FTIR, SEM and SEM-EDX
(Agbeleye, 2017)	clay	Aluminium 6063 alloy – clay (Al-clay) composites	Tribological properties
(Jabareen, 2018)	Coated clay	antimony oxide-coated clay/ polypropylene composites	Thermal, structural and tensile properties
(Liu, Y. 2019)	corn stalk waste	corn stalk waste as potential reinforcement in polymer composites	Chemical, surface morphological and mechanical performances
(Asgari, 2019)	SiC	AZ91 magnesium-alloy chips/SiC	Mechanical properties
(Erdoðan, 2019)	Slag wastes	Epoxy composite filled with industrial wastes	Friction and wear behavior
(Vigneshwaran, 2019)	Red mud	Red mud as a filler and sisal fibre as the reinforcement in a polyester matrix	Mechanical strength and water absorption.

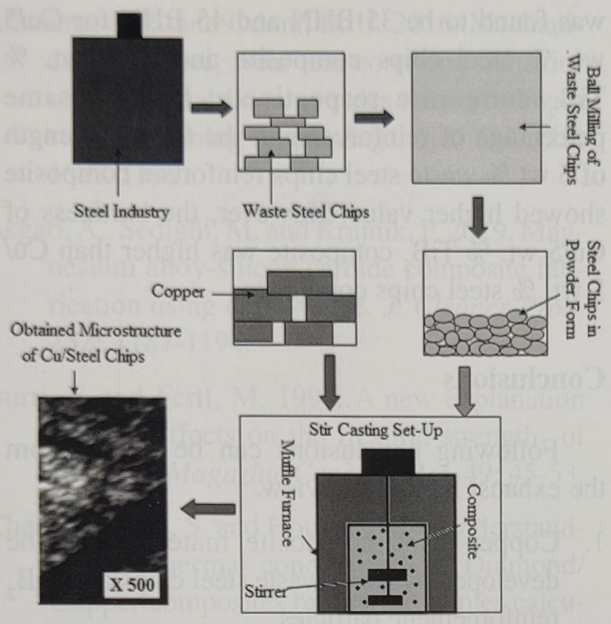

Fig. 1. *Development of Cu/Waste Steel Chips Composite*

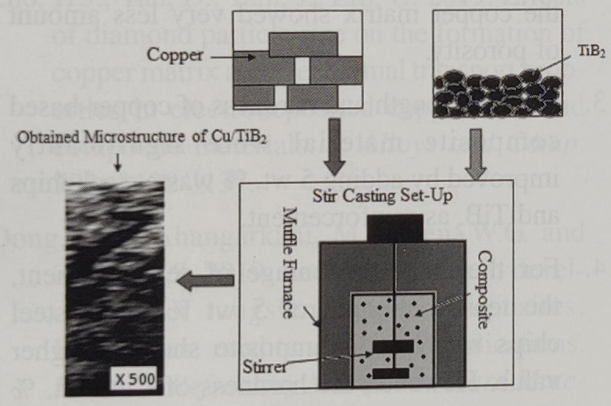

Fig. 2. *Development of Cu/TiB_2 Composite*

sectors where high strength and hardness were required. But, due to its low ductility and strength, it was a big challenge to use it in industrial application. However, nowadays various researchers developed copper based composite with various reinforcement material and showed that cooper based composite materials mechanical properties could be improved by using various reinforcement materials.

Figure 3 showed representative SEM micrograph of Cu/5 wt. % steel chips metal matrix composite. Microstructure results showed the fair distribution of waste steel chips in the copper base matrix material. Microstructure results also showed that waste steel chips in powder form can be used successfully in the copper-based matrix material. Figure 4 showed the SEM image of the surface morphology of Cu/5 wt. % steel chips after the electrochemical test in 3.5 wt% NaCl solution.

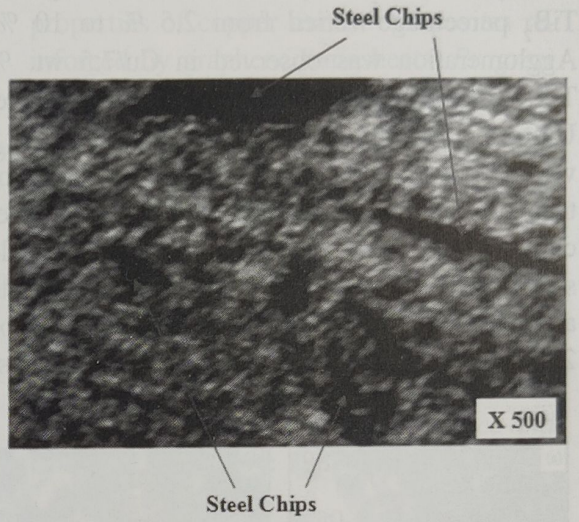

Fig. 3. *SEM micrograph of Copper/5 wt. % Steel Machining Chips*

Fig. 4. *SEM image of the Surface Morphology of Cu/5 wt. % Steel Chips after the Electrochemical Test in 3.5 wt% NaCl Solution*

Alaneme, (2016) also analyzed the corrosion behaviour of Cu/5 wt. % steel chips metal matrix composite. They reported that corrosion of the stainless steel reinforced copper matrix composites in chloride media began at the copper matrix at sites independent of the stainless steel fibers or stainless steel/copper interface. They

noted that pitting of the stainless steel fibers only appeared much later. This they held was a good indication of sound bonding at the interface between the stainless steel fibers and the copper matrix.

Figure 5 shows the microstructure image of Cu/5 wt. % TiB_2 composite material. Weight of TiB_2 percentage varied from 2.5 % to 10 %. Agglomeration was observed in Cu/7.5 wt. % TiB_2 composite and Cu/10 wt. % TiB_2 composite. Uniform distribution can be observed in Cu/ 5 wt. % TiB_2 composite. Comparative study of tensile strength and hardness for 5 wt. % steel chips and TiB_2 are shown in Figure 6. Tensile strength for Cu/5 wt. % steel chips composite and Cu/5 wt. % TiB_2 composite was found to be 220 MPa and 215 MPa respectively. Hardness

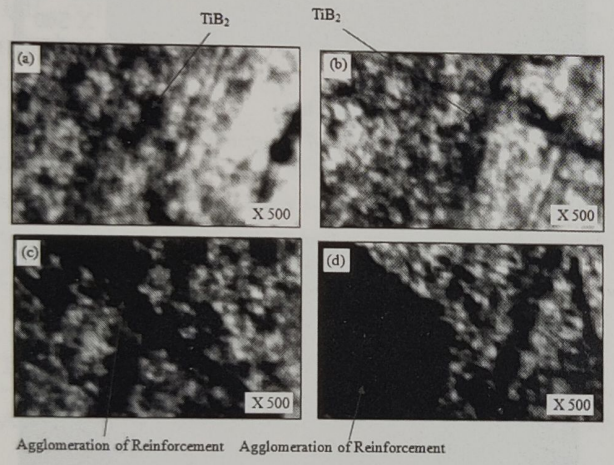

Fig. 5. *Microstructure of Copper/5 wt. % TiB_2 Composite Material*

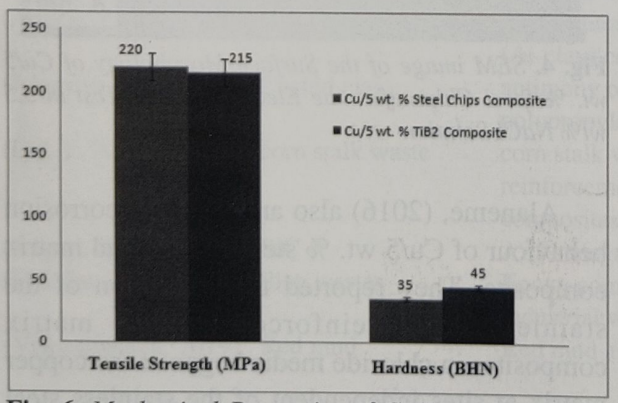

Fig. 6. *Mechanical Properties of Cu/5 wt. Steel Chips Composites and Cu/5 wt. % TiB_2 Composites*

was found to be 35 BHN and 45 BHN for Cu/5 wt. % steel chips composite and Cu/5 wt. % TiB_2 composite respectively. For the same percentage of reinforcement, the tensile strength of 5 wt % waste steel chips reinforced composite showed higher value. However, the hardness of Cu/5 wt. % TiB_2 composite was higher than Cu/ 5 wt. % steel chips composite.

Conclusions

Following conclusions can be drawn from the exhaust literature review.

1. Copper-based composite materials can be developed by using waste steel chips and TiB_2 reinforcement particles.
2. Waste steel chips and TiB_2 with 5 wt. % in the copper matrix showed very less amount of porosity.
3. Tensile strength and hardness of copper-based composite material were significantly improved by adding 5 wt. % waste steel chips and TiB_2 as reinforcement.
4. For the same percentage of reinforcement, the tensile strength of 5 wt % waste steel chips reinforced composite showed higher value. However, the hardness of Cu/5 wt. % TiB_2 composite was higher than Cu/5 wt. % steel chips composite.

References

Afifeh, M., Hosseinipour, S. and Jamaati, R. 2019. Nanostructured copper matrix composite with extraordinary strength and high electrical conductivity produced by asymmetric cryorolling. *Materials Sci. Engin: A.* **763:** 138146.

Agbeleye, A.A., Esezobor, D.E., Balogun, S.A., Agunsoye, J.O., Solis, J. and Neville, A. 2017. *J. King Saud U.y – Sc. https://doi.org/10.1016/j.jksus.2017.09.002.*

Alaneme, K.K. and Odoni, B. U. 2016. Mechanical properties, wear and corrosion behavior of copper matrix composites reinforced with steel machining chips. *Engi. Sci. Tech.* **19**: 1593-1599.

Asgari, A., Sedighi, M. and Krajnik, P. 2019. Magnesium alloy-silicon carbide composite fabrication using chips waste. *J. Cleaner Prod.* **232:** 1187-1194.

Burri, F. and Fertl, M. 1997. A new explanation for size effects on the flexural strength of concrete. *Magazine Concrete Res.* **49:** 45-53.

Chen, L., Chen, S. and Hou, Y. 2019. Understanding the thermal conductivity of Diamond/ Copper composites by first-principles calculations. *Carbon.* **148:** 249-257.

Cho, H.J., Yan, D., Tam, J., Erb, U. 2019. Effects of diamond particle size on the formation of copper matrix and the thermal transport properties in electrodeposited copper-diamond composite materials. *J. Alloys and Comp.* **791:** 1128-1137.

Dong, L.L., Ahangarkani, M., Chen, W.G. and Zhang, Y.S. 2019. Recent progress in development of tungsten-copper composites: Fabrication, modification and applications. *Intern. J. Refractory Metals and Hard Materials*. **75:** 30-42.

Du, Y. and Zhang, X.B. 2009. Heuristics for the one dimensional cutting stock problem with limited multiple stock lengths. *Oper. Res.* **36:** 2074-2081.

Erdoðan, A., Gök, M. S., Koç, V. and Günen, A. 2019. Friction and wear behavior of epoxy composite filled with industrial wastes. *J. Cleaner Production.* **237:** 117588.

Gladkovsky, S.V., Kuteneva, S.V. and Sergeev, S.N. 2019. Microstructure and mechanical properties of sandwich copper/steel composites produced by explosive welding. *Materials Characterization.* **154:** 294-303.

Gorbatyuk, S., Pashkov, A. and Chichenev, N. 2019. Improved Copper-Molybdenum Composite Material Production Technology. *Materials Today: Proc.* **11:** 31-35.

He, X., Zou, G., Xu, Y., Zhu, H., Jiang, H., Jiang, X., Xia, W., Chen, J., Wu, J. and Yang, S. 2018. Nano-mechanical and tribological properties of copper matrix composites reinforced by graphene nanosheets. *Progress in Natural Sci.: Materials Inter.* **28:** 416-421.

Jabareen, A. 2018. Properties of antimony oxide-coated clay/polypropylene composites. *Materials Sci. Engi: B.* **236:** 18-23.

Kavaliauskas, •., Marcinauskas, L., Milieška, M., Valinèius, V., Baltušnikas, A. and •unda, A. 2019. Effect of copper content on the properties of graphite-copper composites formed using the plasma spray process. *Surface and Coatings Tech.*, **364:** 398-405.

Liang, S., Li, W., Jiang, Y., Cao, F., Dong, G. and Xiao, P. 2019. Microstructures and properties of hybrid copper matrix composites reinforced by TiB whiskers and TiB_2 particles. *J. Alloys and Comp.* **797:** 589-594.

Liu, Q., Liu, Y., Tang, S., Cheng, J., Chen, Y., Wang, F., Lv, Z. and Qu, X. 2019. Effects of morphological characteristics of graphite fillers on the thermal conductivity of the graphite/copper composites fabricated by vacuum hot pressing sintering. *Vacuum.* **167:** 199-206.

Liu, R., Luo, G., Li, Y., Zhang, J., Shen, Q. and Zhang, L. 2019. Microstructure and thermal properties of diamond/copper composites with Mo_2C in-situ nano-coating. *Surface and Coatings Tech.* **360:** 376-381.

Liu, Y., Lv, X., Bao, J., Xie, J., Tang, X., Che, J., Ma, Y. and Tong, J. 2019. Characterization of silane treated and untreated natural cellulosic fibre from corn stalk waste as potential reinforcement in polymer composites. *Carbohydrate Polymers.* **218:** 179-187.

Nadoushani, Z.S.M. and Akbarnezhad, A. 2015. Effects of structural system on the life cycle carbon footprint of buildings. *Energy Build.* **102:** 337-346.

Nagdev R, Mahapatra S.K., Singh S.K., Yadav R.P., Surya J.N. 2018. Role of Soil Clays for Watershed Management in Mewat Region of Haryana. *Clay Res.* **37:** 23-32.

Nazeer, F., Ma, Z., Gao, L., Wang, F., Khan, M. A. and Malik, A. 2019. Thermal and mechanical properties of copper-graphite and copper-reduced graphene oxide composites. *Composites Part B: Engin.* **163:** 77-85.

Pavlovic, A. and Fragassa, C. 2011. Sustainable structural design methodologies. *Pract Struct Des Constr.* **16:** 186 -190.

Ropota, I. et al. 2013. Recycling solid wastes as polymer composites. *Studia Universitatis Babes&˜-Bolyai. Chemia.* **58(4):** 213-225.

Sapate, S.G. 2008. A heuristic for the one dimensional cutting stock problem with pattern reduction. *Proc Inst Mech Part : J Eng Manuf.* **222:** 677-685.

Saurabh, K., Manjaiah, K.M., Datta, S.C. and Kumar, R. 2015. Preparation and Characterization of Nanoclay Polymer Composites (NCPCs) Loaded with Urea. *Clay Res.* **34:** 80-90.

Thankachana, T., Prakash, K.S. and Kavimani, V. 2019. Investigating the effects of hybrid reinforcement particles on the microstructural, mechanical and tribological properties of friction stir processed copper surface composites. *Composites Part B: Engi.* **174:** 107057.

Vigneshwaran, S., Uthayakumar, M. and Arumugaprabu, V. 2019. Development and sustainability of industrial waste-based red mud hybrid composites. *J. Cleaner Prod.* **230:** 862-868.

Wang, J., Guo, L., Lin, W., Chen, J., Zhang, S., Chen, S., Zhen, T. and Zhanga, Y. 2019. The effects of graphene content on the corrosion resistance, and electrical, thermal and mechanical properties of graphene/copper composites. *New Carbon Materials.* **34:** 161-169.

Zhang, X., Shi, C., Liu, E., Zhao, N. and He, C. 2019. High-strength graphene network reinforced copper matrix composites achieved by architecture design and grain structure regulation. *Materials Sci. Engi.: A.* **762:** 138063.

Zhou, X., Hu, Z. and Yi, D. 2019. Enhancing the oxidation resistance and electrical conductivity of alumina reinforced copper-based composites via introducing Ag and annealing treatment. *J. Alloys and Comp.* **787:** 786-793.

(Received: 06 May 2019, Accepted: 16 September 2019)

Clay Research, Vol. 38, No. 1, pp. 19-28 (2019)

Synthesis of Chitosan-g-Biomass Ash/Graphene Oxide Nanocomposite for the Removal of Copper and Chromium from Industrial Waste Water

SHIVANGI OMER*, AJAY SINGH AND SHALINI UPADHYAY

School of Applied and Life Sciences, Uttaranchal University, Dehradun Uttarakhand, India

Abstract–*Biomass ash (BA) obtained as a byproduct from biomass feedstock shows adsorption capacity for heavy metals and could be economical and environment friendly adsorbent. Chitosan (Cs) and Graphene oxide (GO) are efficient adsorbent for removal of dyes, metal ions and toxic compounds. When biomass ash is used as nanocomposite formation along with Chitosan and Graphene Oxide then its adsorption capacity is enhanced. In the present work, Chitosan grafted Biomass ash on Graphene oxide base nanocomposite adsorbent (Cs-g-BA/GO) is synthesized for the effective removal of Cu (II) and Cr (VI) metal ions present in industrial waste water. They were characterized by FTIR, UV, FESEM and adsorption was studied by employing AAS with variables like pH, Adsorbent dose and contact time. The results showed that Cs-g-BA/GO nanocomposite is an efficient adsorbent with 69.5 % for Cu(II) and 74.7 % for Cr (VI) at pH 4.5 and 5 respectively. The optimum adsorbent dose was 0.12 g l^{-1} at pH 5 with removal efficiency was 80.0 % and 82.6 % for Cu (II) and Cr (VI) respectively at a contact time of 90 min. Chitosan-g-Biomass ash/ Graphene oxide nanocomposite was significant adsorbent for the removal of Cu(II) and Cr(VI) metal ions present in waste water.*

Keywords: Adsorption, Decontamination, Grafting, Heavy metal, Industrial affluent.

Toxic heavy metals when discharged into water resources are serious threat to environment and human health due to which it is important to remove them from industrial waste water. Adsorption mechanism serves as a good option for the removal of heavy metals (Xu *et al.,* 2018; Rautaray *et al.,* 2003). The adsorption capacity of adsorbent depends on their chemical stability and high surface area as well as the functional groups present on its surface which represents the binding site to the adsorbate (Ali, 2016; Dula *et al.,* 2014).

Biomass ash obtained as byproducts from biomass feed-stocks show adsorption capacity for heavy metals (Lei *et al.,* 2014; Li *et al.,* 2013, Omer *et al.,* 2019). Their compositions vary widely (Table 1). The global growth of biomass is evaluated between 112 and 220 billion ton yr^{-1} and produces about 95–97% of the world's bioenergy (Vassilev *et al.,* 2012; Demirbas 2005; Fouilland *et al.,* 2010; Zhang *et al.,* 2010). The presence of heavy metals in industrial effluents is widespread in many regions of India including Uttar Pradesh, Uttarakhand, Delhi, Madhya Pradesh (Singh *et al.,* 2006).

Organic polymers such as chitosan(Ali, 2016), sodium alginate (Park *et al.,* 2004), inorganic adsorbents such as activated carbon (Acharya *et al.,* 2009), magnetite (Chowdhury *et al.,* 2010) and recently graphene oxide (GO) (Kumar *et al.,* 2013) have been used as adsorbents. Since GO is difficult to separate from treated water, it is bonded with organic materials, such as chitosan, and calcium alginate (Chowdhury *et al.,* 2014; Sheng *et al.,* 2016) to enhance its adsorption property. Chitosan being

***Corresponding Author Email :** shivangiomer@gmail.com; shivangiomer@uttaranchaluniversity.ac.in

a natural biosorbent causes the fine sediment particles to bind together and is removed during sand filtration. So, GO-chitosan nanocomposite is prepared to overcome obstacles related to adsorbent separation and removal of metal ions such as lead ions (Fan *et al.,* 2013), chromium (Debnath *et al.,* 2014) and other pollutants. Adsorption capacity of biomass ash towards heavy metals is increased after appropriate modification (Silva and Pissetti, 2014; Omer *et al.,* 2019). The modified materials with nanostructures more efficiently remove heavy metals from industrial wastewater (L´etant *et al.,* 2014; Singhand Omer, 2018).

Kirti *et al.,* 2018 reported enhanced adsorption activity of bionanocomposites of biomass- *Cassia fistula* multi-functionalized along with iron oxide nanoparticle (SPION). Hosseinzadeh and Ramin, 2018 reported that a modified composite material of GO with ethylenediamine onto chitosan backbones showed high Cu^{2+} sorption capacity, which is easily separable because of its attachment with magnetic nanoparticles. Another modification has been reported in Poly (vinyl chloride) by cross linking of multifunctional amines (Singh *et al.,* 2010; Singh and Rawat, 2013). Metal ions can also be sensed by sensors which can also be utilized for the removal of heavy metals present in industrial effluents (Upadhyay and Singh, 2019).

Material and Methods

In this study, we synthesized a new adsorbent namely, biomass ash-chitosan-graphene oxide nanocomposite by modification of biomass ash with graphene oxide to combine the adsorption properties onto chitosan backbone for separable convenience, with Glutaraldehydeas cross-linking agent. The batch experiments had been carried out to measure the removal efficiency of synthesized nanocomposite for the removal of chromium and copper ions present in industrial waste water. For this, biomass Ash was collected from local iron foundry, confectionary and Hindustan National Glass and Industries Ltd., Rishikesh. Graphite powder was procured from Rankem and chitosan from Hi Media Laboratories.

Modification of Biomass Ash

In order to maintain a uniform size of Biomass ash (BA), it was mechanically riddled and sieved through 80 mesh and 120 mesh. Biomass was frequently rinsed with distilled water and dried at 100°C. Six gram of BA was mixed with 7.2 g solid NaOH. The mixture grounded into fine powder in order to carryout bleaching process. The mixture was kept at 600°C in muffle furnace for 2 hrs under N_2 atmosphere. Then, 60 mL of deionized water was added and mixture was heated at 100°C for 75 hrs.

Preparation of chitosan support and cellulose immobilization

Activation of chitosan molecule in acetic acid medium: Chitosan solution was prepared by dissolving 2.5 g of chitosan powder into 2% v/v of acetic acid solution under ultrasonic stirring for 1 hr at room temperature following the procedure described by Sheng *et al.* (2016). Then, 2g of modified BA was added to acetic acid activated chitosan Solution at 60°C in hot plate for 2 hrs. Biomass turned dense and coated with Chitosan at 60°C, and then impregnated for 2 hrs.

Preparation of GrapheneOxide

Graphene oxide (GO) was prepared as reported previously (Hummers and Offeman, 1958),2 g of graphite powder was mixed with 1.0 g of $NaNO_3$ and 50 mL of H_2SO_4, and stirred for 30 min at 4°C. After stirring, 10 g of the $K_2Cr_2O_7$ was added as an oxidizing agent to oxidize flake graphite for functionalization and continuous stirred for 120 mins at 35 ± 3°C. Then after, 100 mL of water was added with 50 mL of 30 % H_2O_2 and stirred for 15 min at 100°C.

The color of the mixture turned yellow from thick dense brownish paste. The mixture was sequentially washed and filtered with 100 mL of 5% HCl solution to remove extra MnO_2 and sulfate ions present in the mixture. Separated and dried at 40 ± 5°C in an oven.

Preparation of Cs-g-BA/GO Nanocomposite

To prepare a nanocomposite, 0.5 g of obtained GO homogenously dispersed in 30 mL of water was added to Chitosan grafted Biomass ash mixture with continuous stirring for 6 hrs and stored overnight at room temperature. A dense black colored suspension was obtained. 5 mL of deionized water was added and stirred for 15 mins by which a uniform suspension of GO/BA grafted by Chitosan was obtained and crosslinked by addition of 5 mL of 25% (v/v) Glutaraldehyde as a crosslinking agent (Ali M.E.A., 2018), at 50°C for 3 hrs. A dense, thick and crosslinked product was obtained which was filtered and washed with deionized water and then dried at 40 ± 5°C in an oven.

Instrumentation

Calibration curve was drawn for Cs-g-BA/GO Nanocomposite with blank solution of Cu $(CH_3COO)_2$ and $K_2Cr_2O_7$ by UV-Visible Spectrophotometer (Systronics). Fourier transform infrared (FT-IR) spectra of Cs-g-BA/GO Nanocomposite and biomass ash were recorded using FT-IR spectrometer (Perkin-Elmer 100) at the frequency between 4000 and 625 cm^{-1}. The surface morphology of nanocomposite was studied by Scanning Electron Microscope (Zeiss Ultra Plus 4322). After the equilibration, the residual concentration of Cu(II) and Cr(VI) was determined by Perkin Almer Atomic Absorption Spectrophotometer (AAS-200).

Batch Adsorption Experiments

Synthetic waste water (Cu, Cr) were prepared by dissolving Cu $(CH_3COO)_2$ (0.01 g/l) and $K_2Cr_2O_7$ (0.01 g/l) separately in double distilled water and parameters such as pH, adsorbent dose and contact time were optimized. For each metal, 100 mL of solution with initial concentration of 10 mg/L were stirred together with 1.2 g/L of adsorbent in 100 mL Erlenmeyer flasks in pH range from 2.0 to 8.0. To optimize adsorbent dose, different concentrations of Cs-g-BA/GO adsorbent (0.7, 0.8, 1.0, 1.2, 1.3, 1.5 g/l) were added to each metal solutions under mechanical agitation at 30°C with shaking at 222 rpm for 12 hrs. Contact time were studied with interval upto 240 mins. The initial pH value of the Cu^{2+} and Cr^{6+} solutions were adjusted by adding 1:1 HCl and 1% NaOH solutions. The supernatants were filtered with 0.45 μm membrane and Cu (II) and Cr (IV) concentrations in aqueous phase were determined by Atomic Absorption spectrophotometry.

The absorbed concentration of heavy metal onto Cs-g-BA/GO at the equilibrium (q_e, mg/g) and % adsorption were determined by Eq(1) and Eq(2) respectively (Abdullah., 2018) -

$$q_e = \frac{(C_o - C_e)_{xV}}{m} \quad .. (1)$$

$$\% \text{ adsorption} = \frac{C_o - C_e}{C_o} \times 100 \quad .. (2)$$

Where V is the volume of the solution (l), m is the mass of the adsorbent (g), Co and Ce are the initial and equilibrium concentrations of heavy metals in aqueous solution (mg/L), respectively.

Results and Discussion

UV adsorption studies

Fig. 1(a) and (b) shows UV-Visible spectra of Cs-g-BA/GO nanocomposite, at different concentration of metal solutions in water at 280 nm for Cu (CH_3COO_2) and 490 nm (for $K_2Cr_2O_7$) regions, which typically grasp attention for changes takes place in Cu $(CH_3COO)_2$ and $K_2Cr_2O_7$ solution before and after adsorption by nanocomposite.

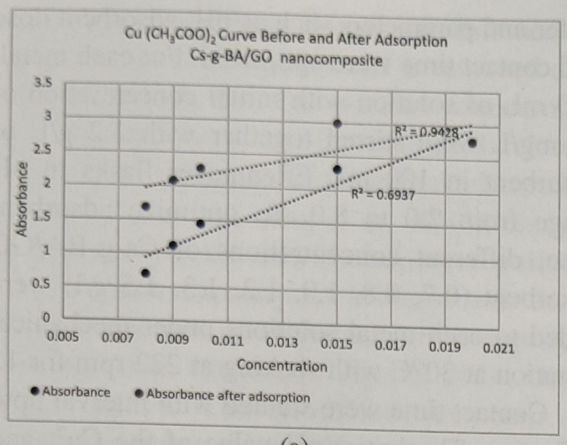

(a)

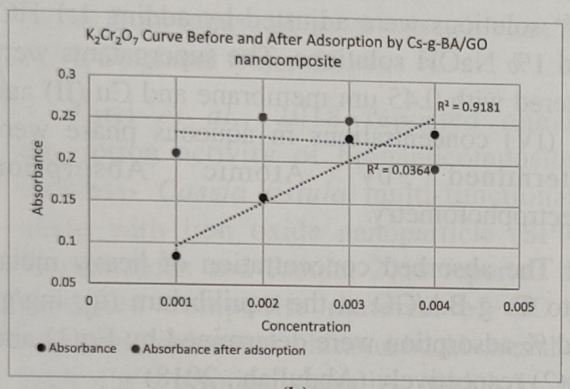

(b)

Fig.1. *Calibration curve of (a) $Cu(CH_3COO)_2$, (b) $K_2Cr_2O_7$ Solutions before and after adsorption by Cs-g-BA/GO nanocomposite.*

SEM analysis

Fig. 2 represents SEM images of Biomass ash (a, b) and Cs-g-BA/GO nanocomposite (c, d). The presence of graphene nanosheets in nanocomposite is observable in microscopic images. Images was recorded in accelerating voltage of 15-20 kV in various magnifications. Energy Dispersive x-ray (EDX) diffraction was used for elemental analysis of modified Biomass ash nanocomposite. High resolution SEM images represents few layers of reduced Graphene oxide with delineation by nanoscalic graphene sheets, which are interconnected with chitosan via copolymerization represented in Fig.2 (c, d). On the other hand, the surface of reduced graphene oxide turned into rough, crumpled which is consist homogeneously dispersed fine fiber like structure spread all over the surface. Fig. 2 (e, f) indicates that the presence of Chitosan rapidly increases the porous structure which leads to increased surface area of Cs-g-BA/GO nanocomposite.

Fig. 2 (g) depicted, the elemental analysis of Cs-g-BA/GO nanocomposite with the presence

Table 1. *Chemical composition of Biomass ash*

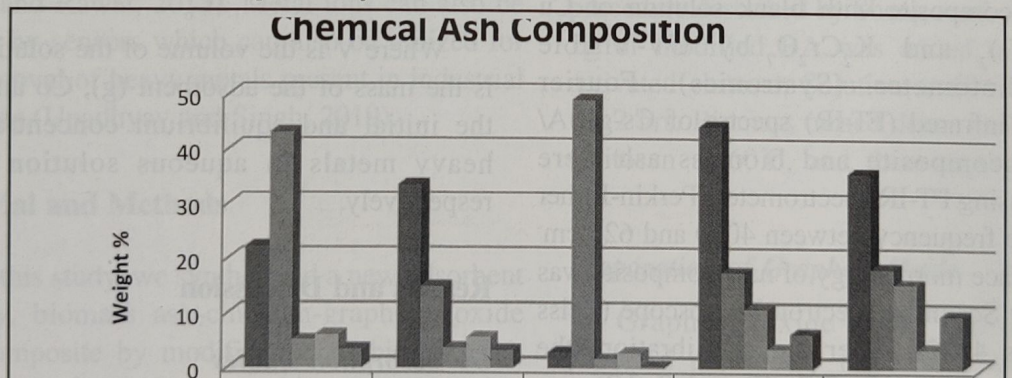

	Wood and woody biomass	Agricultural biomass	Animal biomass	Mixture of biomass	Contaminated biomass
Silicon dioxide	22.22	33.39	2.9	44.19	35.73
Calcium oxide	43.03	14.86	49.04	17.48	18.3
Aluminium oxide	5.09	3.66	1.69	10.82	15.41
Magnesium oxide	6.07	5.62	2.75	3.52	3.6
Ferric oxide	3.44	3.26	0.35	6.34	9.78

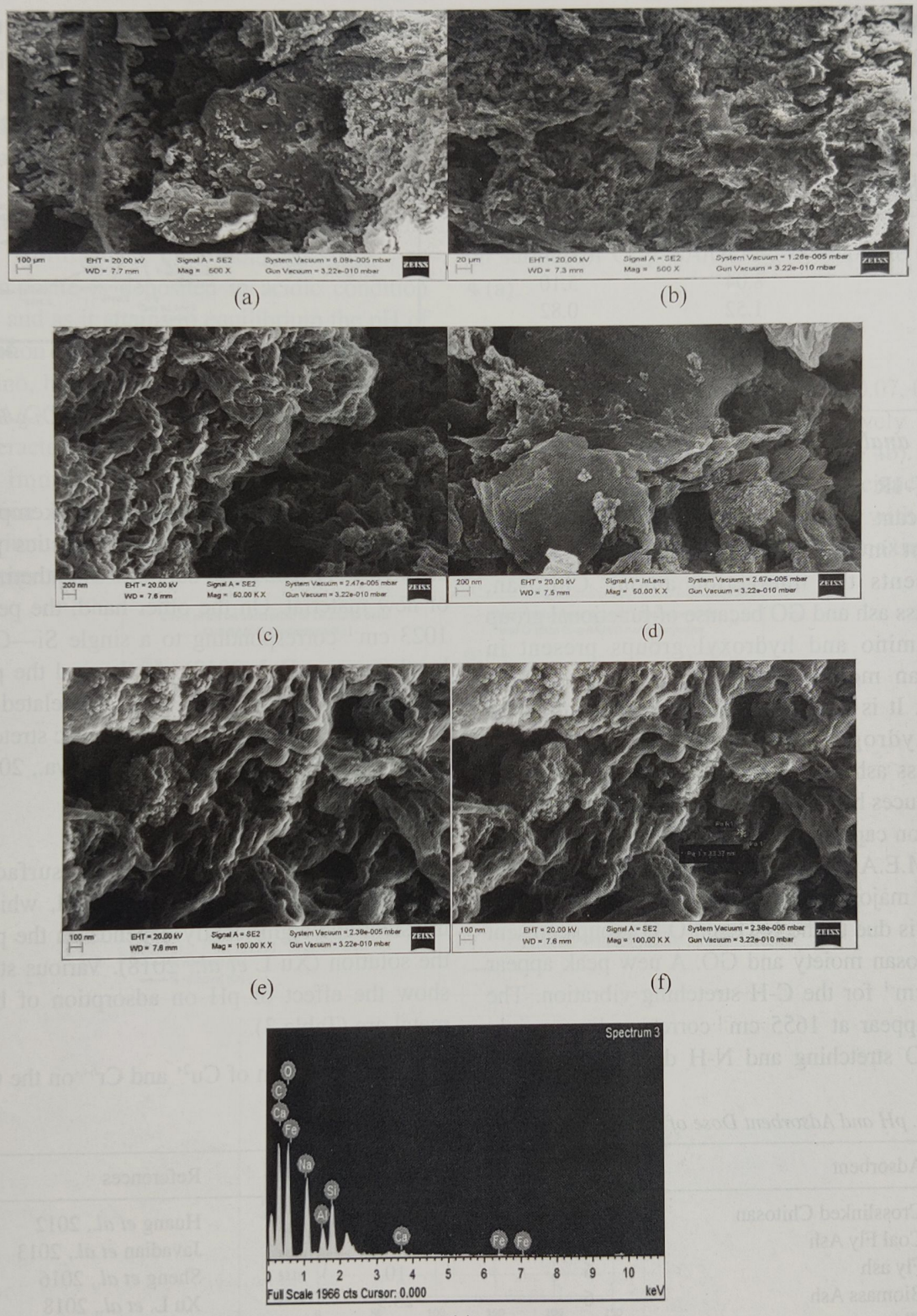

Fig. 2. *SEM images of: (a) Biomass ash, (b) Biomass ash (High magnification), (c) and (d) Cs-g-BA/GO nanocomposite with GO nanosheets, (e) and (f) Polymeric material over GO nanosheets, (g) EDX spectrum of elemental analysis composition of Cs-g-BA/GO nanocomposite.*

of Carbon (53.55%), Oxygen (38.58%), Sodium (5.10%) with high content (Table 2).

Table 2. *Elemental composition of Cs-g-BA/GO nanocomposite obtained by EDX*

Element	Weight (%)	Atomic (%)
C	44.06	53.55
O	42.28	38.58
Na	8.04	5.10
Al	1.52	0.82
Si	3.21	1.67
Ca	0.38	0.14
Fe	0.52	0.14

FT-IR analysis

FT-IR spectroscopy is a well-known significant tool for analyzing functional group present in the nanocomposite. Fig. 3(a, b) represents the interaction among Chitosan, Biomass ash and GO because of functional group like amino and hydroxyl groups present in chitosan moiety which contains polycationic nature. It is also leads to electrostatic attraction and hydrogen bonding between Chitosan, Biomass ash and GO present in nanocomposite. It produces homogenous dispersion and increased adhesion capability of composite with metal ions (Ali M.E.A., 2018). In the spectrum Fig.3(b) shows major characteristic peaks at 3306 cm^{-1}, which is due to the N-H and O-H groups present in chitosan moiety and GO. A new peak appear 2940 cm^{-1} for the C-H stretching vibration. The peak appear at 1655 cm^{-1} corresponding mainly to C=O stretching and N-H deformation band,

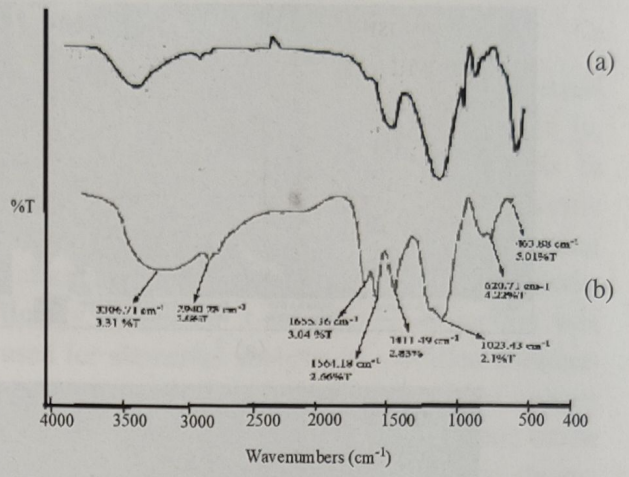

Fig. 3. *IR spectrum of – (a) Biomass Ash (b) Cs-g-BA/GO nanocomposite.*

for amide II of the peptide bond (kemp, W., Palgrave 3rd edition). The characteristics peaks at 1564, 1411, 1023 cm^{-1} supports a synthetization of new material. On the other hand, the peak at 1023 cm^{-1} corresponding to a single Si—O—Si band (Launer, P. J. 2013). At the end the peaks corresponding to 620, 463 cm^{-1} are related with Fe–O bond and Al-O/Si-O asymmetric stretching vibrations, respectively (Shopska Maya., 2013).

Effect of pH

The studies indicate that the surface of biomass ash is a negatively charged, which is transient and significantly depends on the pH of the solution (Xu L *et al.,* 2018). Various studies show the effect of pH on adsorption of heavy metal are (Table 3).

The adsorption of Cu^{2+} and Cr^{6+} on the Cs-g-

Table 3. *pH and Adsorbent Dose of various adsorbents*

S.No.	Adsorbent	pH	Adsorbent dose (g/l)	References
1.	Crosslinked Chitosan	5	0.1	Huang *et al.,* 2012
2.	Coal Fly Ash	5	0.08	Javadian *et al.,* 2013
3.	Fly ash	6	10	Sheng *et al.,* 2016
4.	Biomass Ash	6	23.9	Xu L. *et al.,* 2018
5.	Chitosan	6	0.25	Maity *et al.,* 2018
6.	Chitosan-CDTA-GO	3.5	2	Ali *et al.,* 2018
7.	Coal fly ash/Chitosan	5	–	Zang *et al.,* 2018
8.	Magnetic Chitosan/ GO	8	–	Hosseinzadeh *et al.,* 2018

BA/GO nanocomposite was analyzed and found to be pH-dependent. The pH ranges from 2 to 7 was used to study and effective removal occured at pH 4.5 for Cu(II) and at pH 5.0 for Cr(VI) after reaching at equilibrium at a initial adsorbent dose of 120mg/100 mL at room temperature and pH higher than 6, minimal changes occured. The metal solutions become alkaline as nanocomposite is deposited in acidic condition (pH 5), and as it attains to equilibrium the pH of the solution reached to neutral. It may be due to, the amino, hydroxyl and amide group present in Cs-g-BA/GO nanocomposite were readily ionized and interacted with metal ions leading to change in pH immediately in basic range. As the adsorption interaction occured and reached to equilibrium, again flipping of pH occured from basic range to neutral.

With the increase of pH, the negative charge on the surface of the material is improved, leading to improve the electrostatic force between adsorbent and adsorbate. The maximum adsorption efficiency of Cu^{2+} and Cr^{6+} were observed pH 4.5 and 5 respectively can be attributed to precipitation of Cu^{2+} and Cr^{6+} ions on surface of Cs-g-BA/GO nanocomposite (Fig. 4 (a).

Effect of adsorbent dose

The range of adsorbent dose were 0.07, 0.08, 0.10, 0.12, 0.13 and 0.15g respectively at a contact time of 60 min at pH 5 (Fig. 4b). The results showed that the removal efficiency of Cu(II) and Cr(VI) were increased with the increase the adsorbent dose. The maximum

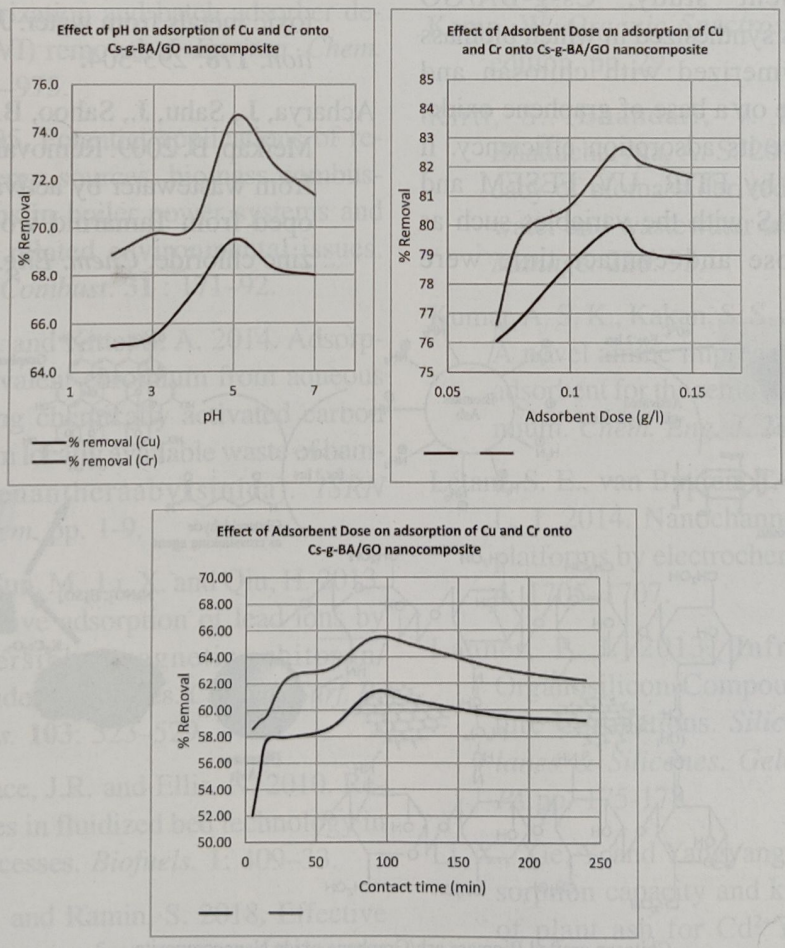

Fig. 4. *Effect of (a) pH, (b) Adsorbent dose, (c) Contact time on adsorption of Cu(II) and Cr(VI) onto Cs-g-BA/GO nanocomposite*

removal efficiency obtained at a dosage of 0.12 g/l with 80% removal of Cu (II) ions and 82.6% of Cr(VI) ions respectively.

Effect of Contact time

Fig. 4(c) represents the influence of contact time on Cu(II) and Cr(VI) adsorption. Appropriate time is required to interact nanocomposite with metal ions. The range of contact time for study was upto 240 minutes. The maximum biosorption efficiency was obtained at a contact time of 120 minutes with percent removal of 60.69% for Cu(II) ions and 64.85% for Cr(VI) ions respectively.

Conclusion

In the present study, Cs-g-BA/GO nanocomposite was synthesized in which biomass ash were co-polymerized with chitosan and formed a composite on a base of graphene oxide, in order to enhance its adsorption efficiency. It was characterized by FTIR, UV, FESEM and SEM-EDX and AAS with the variables such as pH, adsorbent dose and contact time were optimized. The obtained results showed that Cs-g-BA/GO nanocomposite was an efficient adsorbent with removal efficiency of 80.0 % for Cu (II) and 82.6 % for Cr (VI). Optimum adsorbent dose of 0.12 g/l was obtained at a pH 4.5 for Cu(II) and pH 5 for Cr(VI). The optimized contact time of 90 mins was obtained for maximum removal. Overall, Cs-g-BA/GO Nanocomposite was found to be effective and efficient adsorbent for the removal of Cu(II) and Cr(VI) metal ions present in waste water.

References

Abdullah, A.., Khan, M.A., Otero, M., Siddiqui, M.R., Jeon, B. and Batoo, K.M. 2018. A Magnetic Nanocomposite produced from Camel bones for an efficient adsorption of toxic metals from water. *J. Cleaner Production.* **178**: 293-304.

Acharya, J., Sahu, J., Sahoo, B., Mohanty, C. and Meikap, B. 2009. Removal of chromium (VI) from wastewater by activated carbon developed from Tamarind wood activated with zinc chloride. *Chem. Eng. J.* **150**: 25–39.

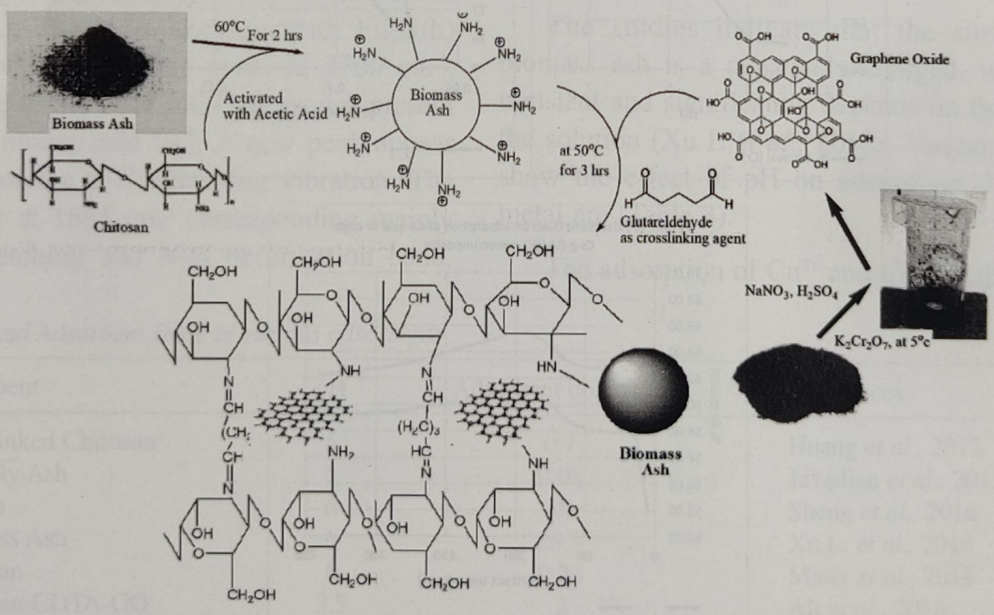

Chitosan grafted Biomass ash/Graphene oxide Nanocomposite

Fig. 5. Graphical Representation for preparation of Cs-g-BA/GO Nanocomposite

Ali, Mohamed, E. A. 2018. Synthesis and adsorption properties of chitosan- CDTA-GO nanocomposite for removal of hexavalent chromium from aqueous solutions. *Arabian J. Chem.* **11**: 1107-1116.

Chowdhury, S. and Balasubramanian, R. 2014. Recent advances in the use of graphene-family nanoadsorbents for removal of toxic pollutants from waste water. Adv. *Colloid Interface Sci.* **204**: 35-56.

Chowdhury, S. R. and Yanful, E. K. 2010. Arsenic and chromium removal by mixed magnetite–maghemite nanoparticles and the effect of phosphate on removal. *J. Environ. Manage.* **91**: 2238–2247.

Debnath, S., Maity, A., and Pillay, K. 2014. Magnetic chitosan–GO nanocomposite: Synthesis, characterization and batch adsorber design for Cr(VI) removal. *J. Environ. Chem. Eng.* **2** : 963–973.

Demirbas, A. 2005. Potential applications of renewable energy sources, biomass combustion problems in boiler power systems and combustion related environmental issues. *Prog Energ Combust.* **31** : 171–92.

Dula, T., Siraj, K. and Kitte, S. A. 2014. Adsorption of hexavalent chromium from aqueous solution using chemically activated carbon prepared from locally available waste of bamboo (Oxytenantheraabyssinica). *ISRN Environ. Chem.* pp. 1-9.

Fan, L., Luo, C., Sun, M., Li, X. and Qiu, H. 2013. Highly selective adsorption of lead ions by water-dispersible magnetic chitosan/graphene oxide composites. *Colloids Surf. B: Biointerfaces.* **103**: 523–529.

Fouilland, T., Grace, J.R. and Ellis, N. 2010. Recent advances in fluidized bed technology in biomass processes. *Biofuels.* **1**: 409–33.

Hosseinzadeh, H. and Ramin, S. 2018. Effective removal of copper from aqueous solutions by modified magnetic chitosan/graphene oxide nanocomposites. *J. of Biological Macromolecules.* **113** : 859-868.

Huang, R., Yang, B. and Liu, Q. 2013. Removal of Chromium(VI) Ions from Aqueous Solutions with Protonated Crosslinked Chitosan. *J. Applied. Polym. Sci.* **129**: 908-915.

Hummers, W.S. and Offeman, R.E. 1958. Preparation of Graphitic Oxide. *J. Am. Chem. Soc.* **80**: 1339-1339.

Javadian, H., Ghorbani, F., Tayebi, H. and Asl, S. H. 2015. Study of the adsorption of Cd (II) from aqueous solution using zeolite-based geopolymer, synthesized from coal fly ash; kinetic, isotherm and thermodynamic studies.*Arabian Journal of Chemistry*. **8**:837-849.

Kemp, W. *Organic Spectroscopy*, Palgrave. 3rd edition. pp. 29.

Kirti, S., Bhandari, V. M., Jena, J. and Bhattacharyya, A. S. 2018. Elucidating efficacy of biomass derived nanocomposites in water and wastewater treatment. *J. Environ. Manage.* **226**: 95.

Kumar, A. S. K., Kakan, S. S. and Rajesh, N. 2013. A novel amine impregnated graphene oxide adsorbent for the removal of hexavalent chromium. *Chem. Eng. J.* **230**: 328–337.

Létant, S. E., van Buuren, T. W., and Terminello, L. J. 2014. Nanochannel arrays on silicon platforms by electrochemistry. *Nano Letters.* **4**: 1705–1707.

Launer, P. J. 2013. Infrared Analysis of Organosilicon Compounds: Spectra-Structure Correlations. *Silicon Compounds: Silanes & Silicones. Gelest, Inc Morrisville, PA*.pp. 175-178.

Li, X., Xie, Y. and Yangyang. 2013. Study on adsorption capacity and kinetic characteristics of plant ash for Cd^{2+} in sewage water. *J. Northeast Agri. Univ.* **44**: 39–42.

Maity, J. and Ray, S. K. 2018. Chitosan based nano composite adsorbent—Synthesis, characterization and application for adsorption of binary mixtures of Pb(II) and Cd(II) from water. *Carbohydrate Polymers*. **182**: 159-171.

Omer, S., Singh, A., Rose, S. and Singhal, A. 2019. Adsorption studies on chitosan and guargum nanocomposite by application of agriculture waste – A review. *Inter. J. Res. Anal. Rev.* **6**: 1059-1062.

Park, H.G. and Chae, M. Y. 2004. Novel type of alginate gel-based adsorbents for heavy metal removal. *J. Chem. Technol. Biotechnol.* **79**: 1080–1083.

Rautaray, S. K., Ghosh, B.C. and Mittra, B. N.2003. Effect of fly ash, organic wastes and chemical fertilizers on yield, nutrient uptake, heavy metal content and residual fertility in a rice– mustard cropping sequence under acid lateritic soils. *Bioresource Tech.* **90**:275–283.

Sheng, G., Zhu, S., Wang, S. and Wang, Z. 2016. Removal of dyes by a novel fly ash-chitosan-graphene oxide composite adsorbent. *RSC Advances*. **6**: 17987

Shopska, M., Cherkezova-Zheleva, Z., Paneva, D., Iliev, M., Kadinov, G., Mitov, I. and Groudeva, V. 2013. Biogenic iron compounds: XRD, Mossbauer and FTIR study. *Cent. Eur. J. Chem.* **11**: 215-227.

Silva, F. A. B. and Pissetti, F. L. 2014. Magnetic chitosan–GO nanocomposite: Synthesis, characterization and batch adsorber design for Cr(VI) removal. *Journal of Colloid and Interface Science*. **416**: 95– 100.

Singh, A. and Omer, S. 2018. Adsorption of Heavy metal using Biomass ash and Guar gum Nanocomposite from waste water effluent – A review. *SSRN- Elsevier*. **1**:3.

Singh, A. and Rawat, M. S. M. 2013. A Review on Poly(vinyl chloride) and its Modification by Crosslinking and Grafting. *Res. Rev. Polymer.* **4**:73-80.

Singh, A., Rawat, M. S. M. and Pande, C. S. 2010. Chemical Modification and Characterization of Poly (vinyl chloride) by cross linking of multifunctional amines. *J. App. Poly. Sci.* **118**: 876-880.

Singh, A., Saxena, S., Gaur, S. and Chauhan, R.K. 2006. Biological Effect of Heavy metal in drinking water of Shivalik & western UP regions in India. *Chemical Weekly*. pp. 193-197.

Upadhyay, S., Singh, A., Sinha, R., Omer, S. and Negi, K. 2019. Colorimetric Chemosensors for d-metal ions: A Review in the past, present and future prospect. *J. of Molecular Structure*. https://doi.org/10.1016/j.molstruc.2019.05.007.

Vassilev, S. V., Baxter, D., Andersen, L. K. and Vassileva, C.G. 2012. An overview of the composition and application of biomass ash. Part 1. Phase–mineral and chemical composition and classification. *Fuel*. **105**: 40-76.

Xu, L., Cui, H., Zheng, X., Liang, J., Xiangyu, X., Yao, L., Chen, Z. and Zhou, Jing. 2018. Adsorption of Cu^{2+} to biomass ash and its modified product. *Water Sci Technol.* **1**: 115-125.

Zang, L., Qiao, X., Hu, L., Yang, C., Liu, Q., Wei, C. and Liu, C. 2018. Preparation of Magnetic Chitosan Nanoparticles As Support for Cellulase Immobilization. *Ind. Eng. Chem. Res.* **53** : 3448-3454

Zhang, L., Xu, C. and Champagne, P. 2010. Overview of recent advances in thermochemical conversion of biomass. *Energy Convers Manage.* **51:** 969–82.

(Received: 05 July 2019, Accepted: 16 September 2019)

Clay Research, Vol. 38, No. 1, pp. 29-34 (2019)

Response of Waste Egg Shells to Soil Fertility and its Impacts on the Growth of *Vigna mungo* L. Seedling

SUSANTA KUMAR BISWAL[a], TRUSHNA MAYEE PRADHAN[a] AND ATIA ARZOO[b]*

[a]*Department of Chemistry, School of Applied Sciences, Centurion University of Technology and Management, Odisha, India-752050*
[b]*Department of Environmental Science, School of Applied Sciences, Centurion University of Technology and Management, Odisha, India-752050*

Abstract–*Egg shells are one of the solid waste which contribute significantly to environmental pollution by its smell, provides the perfect habitat for flues, damage the nearby environment and also causes some allergies to people working nearby areas when kept for longer time. The novelty of this work is utilization of the waste egg shells in an environment friendly way. Researchers have studied the use of various biomaterials for soil fertility, However there is little report available on the use of egg shells. In the present study it was found that the waste egg shells contain Al_2O_3, SiO_2, SiO_3, CaO, MnO, Fe_2O_3, ZrO_2, Cl, K_2O, etc. which are the essential macro and micronutrients for plants. So waste egg shells can be used as plant fertilizer due to presence of 95% of calcium carbonate which is a potent source of lime to neutralize the pH of acidic soil. It was also found that Vigna mungo L. seeds were grown better in egg shell treated soil that is 10 mm larger than the plant grown in control. From this research, it can be concluded that waste egg shells can fulfil the mineral requirement for the growth of Vigna mungo L. plants as it enhanced the nutrient level in soil.*

Key words: Egg shell, Major and minor nutrient, Acidic soil, Fertilizer, Plant growth

Agriculture is one of the important livelihood in various countries. Due to the use of chemical pesticides and fertilizers, the nature of the soil changes (such pH decreases, accumulation of heavy metals etc.). Thus there is a need to use biomaterials in agriculture that may not only improve the quality of crops but also the quality of the land. Use of waste biomaterials may help reduce the cost also. Environmental pollution at different sites are greatly influenced by the consumption pattern and habits of waste management (Vaccari *et. al.*, 2019). Implementation of waste hierarchy should be needed to manage the waste statistics to reach the circular economy (Ana *et al.*, 2019). The total amount of waste generated throughout the world is around 3.2 billion tons, out of which 70% of waste is not recycled or reused (Tisserant *et. al.*, 2017). On the other hand use of bio fertilizer is environment friendly and also helps to increase the soil fertility for better production and yield of crop. As eggshell powder is a stabilizing materials which improves the properties of soil (Ok *et al.* 2011), these can be used as biofertilizer in the crop field to decrease the plant diseases and improve the productivity of soil.

Egg shells contain significant amount of calcium thus fulfils the amount of calcium in plant. So the use of waste egg shells as an alternative source for correcting soil fertility as a bio-fertiliser and also can reduce the environmental impact favoured by the disposal of this by-product. Therefore the present research work was conducted to study the Response of waste egg shells to soil fertility and its impacts on the growth of *Vigna mungo* L. seedling. The main objectives of this present work is egg shells can supply nutrients to the plant and also helps maintain the pH balance of the soil. It being a

waste biomaterial, involves less cost and creates less problems to the environment.

Materials and Methods

Soil samples were collected from mango garden of Centurion University of Technology and Management, Bhubaneswar, Odisha, India, with having lattitude 20.1756° N and longitude 85.7066° E at 18 cm soil depth using a neat and clean soil auger with four replicates. The samples were collected in polyethylene bags and properly labelled. Then the collected soil samples were taken to the laboratory then sterilized and properly packed in polythene for avoiding microbial contamination and preserved the soil and further analysis has been done as per standard procedure (Saeed and Rafiq, 1980). Then the samples were dried in sun light for about twenty four hour and again dried in an oven at 105°C till complete dehydration. The sample was ground in a mortar pestle then passed through 0.5 mm sieve which was required for elemental analysis. Then the soil samples preserved properly for further analysis. Waste egg shells were collected from different fast food shops and vending zone near Centurion University of Technology and Management, Bhubaneswar, Odisha, India. The physico-chemical parameters of soil like pH, electrical conductivity (E.C.) were measured by electro-potentio method, soil moisture percent (%), water holding capacity were measured by gavimetric method and elemental content (Al_2O_3, SiO_2, SiO_3, CaO, MnO, Fe_2O_3, ZrO_2, Cl, K_2O etc.) of both soil and waste egg shells were analyzed using XRF spectroscopy.

Uniform sized healthy seeds were sterilized with 0.1% $HgCl_2$ for about five minutes and then washed several times with tap water followed by distilled water. The sterilized seeds were germinated in different concentration of egg shell treated soil along with control soil. Seeds were allowed to germinate at room temperature (28 ± 2°C) in darkness for five days. The number of seed germinated in each treatment was counted and radical lengths were also measured.

Percentage of germination was calculated as:

$$\text{Germination (\%)} = \frac{\text{Number of seeds germinated}}{\text{Total number of seeds shown}} \times 100$$

According to Chou *et al.* (1978), The percentage of phytotoxicity of the metal was calculated by the formulae:

$$\text{Phytotoxicity (\%)} = \frac{\text{Redicle length of control} - \text{Radicle length of test}}{\text{Radicle length of control}} \times 100$$

According to Baki and Anderson (1973), Seedling vigour indices were calculated as:

Vigour index = Germination percentage × Length of the embryonic axis

As per the formula proposed by Turner and Marshal (1972), The tolerance indices of the seedlings were calculated as:

$$\text{Tolerance index} = \frac{\text{Radicle length of seed in test}}{\text{Radicle length of control}} \times 100$$

Statistical Analysis: The statistical implication of various chemical composition of pH, electrical conductivity, water holding capacity and percentage of moisture contents were studied utilizing co-variance matrix by Matlab software. The ratio of the final (egg shell mixed soil) values of various parameters and before addition of egg shell were used for the analysis. The p-value less than 0.05 implies significant contributions.

Results and Discussion

Changes in physico-chemical properties of soil : The physico-chemical parameters like pH, electrical Conductivity (E.C.), soil moisture content (%), water holding capacity and different elements/compound contents of a garden soil and garden soil treated with waste egg shells were analysed and both the results were compared (Table 1, 2 and 3).

In this present study, pH of the garden soil sample was found to be increased from 6.54 to 7.38 which is greatly significant change after addition of waste egg shells. Electrical conductivity of the soil sample under consideration was found to be 0.82 mS/cm. The electrical conductivity of soil treated with waste was found to be 0.85 mS/cm which depicted the small increase from initial soil. After addition of waste, Soil moisture was found to be increased from 11.00 % to 11.50% which was not significantly changed. The amount of water that soil can hold is very important for plant growth. The water holding capacity of garden soil and egg shell mixed garden soil were found to be 157.54 ml/kg and 159.32 ml/kg respectively, small increment was found in waste treated soil which is very useful for plant growth. Different

Table 1. *Comparison between different physico-chemical parameters of garden soil and egg shell mixed garden soil*

Parameters	Unit	Garden soil	Egg shell+ Garden soil	p-value
pH		6.542±0.052	7.384±0.012	0.0007
Elecrtrical conductivity (E.C)	mS/cm	0.820±0.003	0.854±0.004	0.0004
Water Holding Capacity	ml/kg	157.542±0.582	159.321±0.562	0.2321
Moisture Content	%	11±0.572	11.502±0.564	0.949

Values of four replicates ± SEM

Table 2. *Comparison between the amount of compounds present in garden soil and egg shell waste mixed soil*

Elements/ compound	Unit	Garden soil	Garden soil mixed with egg shell waste	p-value
Eu_2O_3	%	0.065±0.004	0.079±0.002	8.902
Al_2O_3	%	15.712±0.063	18.714±0.003	3.220
SiO_2	%	66.184±0.062	61.18±0.006	7.250
P_2O_5	%	1.034±0.002	1.011±0.001	0.078
K_2O	%	1.446±0.005	1.964±0.005	1.300
CaO	%	0.138±0.003	4.336±0.002	1.632
TiO_2	%	1.544±0.023	1.812±0.014	7.740
MnO	%	0.145±0.003	0.210±0.003	2.730
Fe_2O_3	%	6.213±0.031	9.216±0.009	1.010
ZrO_2	%	0.145±0.003	0.212±0.002	4.620
SO_3	%	0.663±0.002	0.365±0.008	5.635
Cl	%	0.193±0.002	0.195±0.006	0.126
V_2O_5	%	0.033±0.002	0.033±0.003	0.380
Cr_2O_3	%	0.019±0.009	0.024±0.002	0.007
NiO	%	0.007±0.001	0.011±0.001	0.004
CuO	%	0.010±0.002	0.010±0.001	0.404
ZnO	%	0.014±0.003	0.018±0.001	0.008
Ga_2O_3	%	0.003±0.001	0.004±0.001	0.008
As_2O_3	%	0.001±0.001	0.002±0.001	0.008
Rb_2O_3	%	0.014±0.002	0.013±0.001	0.107
SrO	%	0.013±0.002	0.012±0.003	0.243
Y_2O_3	%	0.003±0.001	0.006±0.001	0.011
Nb_2O_3	%	0.004±0.001	0.005±0.001	0.011
SnO_2	%	0.0094±0.001	0.0096±0.001	0.195

Values of four replicates ± SEM

elemental content of the soil was also analysed. It was found that the different elemental content like Eu_2O_3, Al_2O_3, K_2O, CaO, TiO_2, MnO, Fe_2O_3, ZrO_2, Cl, Cr_2O_3, NiO, ZnO, Ga_2O_3, As_2O_3, Y_2O_3, Nb_2O_3 and SnO_2 increased with addition of waste egg shells which could enhance the soil fertility and help in better plant growth. From Table 3, it was observed that SiO_2 has significant contribution on pH, electrical conductivity, water holding capacity and percentage of moisture content. However, for electrical conductivity Eu_2O_3, Al_2O_3, SiO_2 and Fe_2O_3 were found to have significant effect. So it can be concluded that the waste material can neutralize the pH of soil, which is more beneficial for plants rather than garden soil.

Impact of waste on the germination and growth parameters of Vigna mungo L. : Germination of seed is the most important stage of plant growth and it can be used as a reference for plant development and an indication for early response of plants. The percentage of germination was found to be increased by increasing the weight of waste products. The percentage of germination of seeds from control to 1000 mg/L were found to be increased from 84.76 to 94.02 (Fig. 1). Similarly seedling vigour indices and tolerance indices were found to be increased whereas the percentage of phyto-toxicity was found to be decreased with increasing concentration of waste egg shells (Fig. 2). The root and shoot lengths of germinated seeds were also found in an increasing trend with increasing concentration of waste egg shells (Fig. 3). As Egg shell enhances the soil nutrient content, so it was shown better result in terms of germination and growth of *Vigna mungo* L. seedling. From several reports it was found that the waste egg shell contains high amount of calcium carbonate (Ahmad *et al.* 2012), which acts as an

Table 3. *Co-variance in pH, E.C., WHC and moisture content due to addition of different elemental content*

	pH	E.C.	WHC	Moisture content
Eu2O3	0.561979	0.026774	0.610822	2.478555
Al2O3	0.111676	0.013308	0.128016	0.091534
SiO2	0.033375	0.015007	0.04266	0.001072
P2O5	4.976447	1.486622	6.049847	3.022245
K2O	0.301597	0.382959	0.507031	3.167559
CaO	44.09678	15.40223	54.42798	28.74302
TiO2	0.111189	0.076062	0.15891	0.77601
MnO	1.38049	0.356077	1.652623	1.33225
Fe2O3	0.095122	0.031185	0.119763	0.282564
ZrO2	0.652879	0.767311	0.985689	2.937339
SO3	0.310143	0.096054	0.389275	1.02125
Cl	2.510271	0.443347	2.926425	2.642958
V2O5	4.132004	2.551377	5.650841	12.14887
Cr2O3	10.8212	0.845753	11.98291	33.15438
NiO	20.6631	1.929348	21.63686	61.0416
CuO	19.50786	2.232461	21.39317	66.05747
ZnO	2.571503	5.526185	5.502548	63.44039
Ga2O3	41.30437	9.748988	49.95293	53.56193
As2O3	66.7112	16.95091	79.29292	116.5596
Rb2O3	1.492264	2.883432	2.72692	1.241556
SrO	32.20585	8.681182	39.47683	55.2179
Y2O3	12.50398	15.26622	7.004074	124.4064
Nb2O3	5.361765	1.250462	6.501779	9.491284
SnO2	4.399699	0.945894	4.621647	10.80847

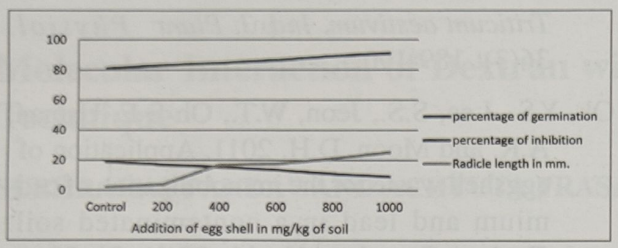

Fig. 1. *Impact of waste egg shells on germination and radicle length of Vigna mungo seeds*

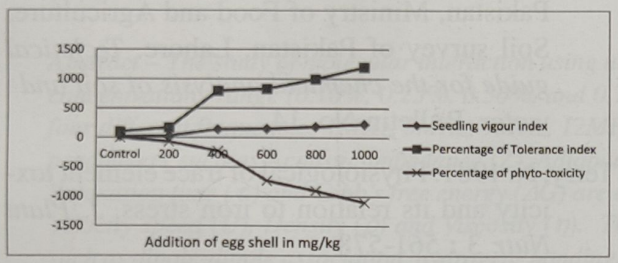

Fig. 2. *Impact of waste egg shells on seedling vigour indices, tolerance indices and percentage of phyto-toxicity of Vigna mungo seeds*

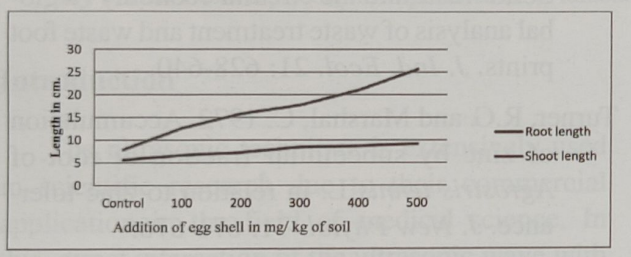

Fig. 3. *Impact of waste egg shells on growth of the Vigna mungo seedlings after 15 days of treatment*

immobilizing agent to fix the metals in the soil (Ok *et al.* 2011). Some metals like iron, copper and zinc are essential for plants and animals. The availability of some metals such as copper, zinc, iron, manganese, molybdenum and nickel varies from region to region and such metals are essential micronutrients (Arzoo and Satapathy, 2017). According to Ok *et. al*, (2011) and Ahmad *et. al.* (2012), egg shell was used for fixing of lead (Pb) and cadmium (Cd) in acidic soils, which ultimately increased the pH of soil towards its neutrality. As the egg shell fixes different beneficial micro or macronutrients in soil that small amount of different metals enhance the plant growth like nickel in *Macrotyloma uniflorum* (Arzoo *et. al.*, 2014), cobalt in *Vigna mungo* L., cadmium in *Triticum aestivum* (Kalita *et. al.*, 1993), Chromium in *Salvia sclera* (Corradi *et. al.*, 1993), food waste in peanut crops (Daud *et. al.*, 2016), cobalt and zinc in *Penisetum americanum* and *Parkinsonia acculata* (Terry, 1981). which argue the confirmation of the result that found in this research that egg shells enhance growth of *Vigna mungo* seedling due to presence of different micro or macro nutrient.

Conclusions

Waste egg shells can be used as fertilizer due to presence of 95% of calcium carbonate and is a potent source of lime which neutralize the pH of acidic soil. The green gram seeds were grown better in egg shell fertilized soil that is 10 mm larger compared to the plant grown in control. So from this research it can be concluded waste egg shells can fulfil the mineral requirement for the plant's growth. Moreover, it is an excellent organic manure for better growth and development of *Vigna mungo* L. plants.

Acknowledgments

We are thankful to Centurion University of Technology and Management, Odisha for providing necessary Laboratory facilities during the course of investigation.

References

Abdul Baki A. A., Anderson, J.D. 1973. Vigour determination in soybean seed by multiple criteria. *Crop Sci.* 3**:** 630-633.

Ahmad, M., Hashimoto, Y., Moon, D.H., Lee, S.S. and Ok, Y.S. 2012. Immobilization of lead in a Korean military shooting range soil using eggshell waste: an integrated mechanistic approach. *J. Hazard. Mater.* 209: 392–401.

Ana, P. and Martinho, G. 2019. Waste hierarchy index for circular economy in waste manage-

ment. *J. Waste Management*. 95: 298-305.

Arzoo, A. and Satapathy, K.B. 2017. A review on sources of heavy metal pollution and its impacts on environment. *Int. J. Cur. Adv. Res.* 6(12): 8098-8102.

Arzoo, A., Nayak, S.K., Mohapatra, A. and Satapathy, K.B. 2014. Impact of nickel on germination, seedling growth and biochemical changes of *Macrotyloma uniflorum* (Lam.) verdc., *Int. j. Biosci.* 5 (9): 321-331.

Chou, C.H., Chiang, Y.C. and Kao, C. I. 1978. Impacts of water pollution on crop growth in Taiwan. Phytotoxic natures of six rivers and twenty seven industrial waste water in Kaoshiung area, Taiwan. *Bot. Bul. of Acad. Sinica.* 19: 107-124.

Corradi, M.G., Blanchi, A. and Albasini, A. 1993. Chromium toxicity in *Salvia sclarea*. Effects of hexavalent chromium on seed germination and seedling development. *Env. and Exp. Bot.* 33(3) : 405-413.

Daud Noorzaidi, M., Ramli, N. and Ambong, S. 2016. Producing fertilizer from waste recycling using Barkeley and Bokashi method. *Int. Sci. Res. J.* 72: 75-83.

Kalita, M.C., Devi, P. and Bhattacharya, I. 1993. Effect of cadmium on seed germination, early seedling growth and chlorophyll content of *Triticum aestivum*. *Ind. J. Plant Physiol.* 36(3): 189-190.

Ok, Y.S., Lee, S.S., Jeon, W.T., Oh S-E, Usman, A.R. and Moon, D.H. 2011. Application of eggshell waste for the immobilization of cadmium and lead in a contaminated soil. *Environ Geo chem Health*. 33(1): 31–39

Saeed, G. and Rafiq, M. 1980. Government of Pakistan, Ministry of Food and Agriculture, Soil survey of Pakistan, Lahore. *Technical guide for the chemical analysis of soil and water*, Bulletin No. 14.

Terry, N. 1981. Physiological of trace element toxicity and its relation to iron stress. *J. Plant Nutr.* 3 **:** 561-578

Tisserant, A., Pauliuk, S., Merciai, S., Schmidt, J., Fry, J., Wood, R. and Tukker, A. 2017. Solid waste and the circular economy : a global analysis of waste treatment and waste foot prints. *J. Ind. Ecol*. 21: 628-640.

Turner, R.G. and Marshal, C. 1972. Accumulation of zinc by subcellular fraction of root of *Agrostris tennis* L. in relation to zinc tolerance. *J. New Phytol.* 71: 671-676.

Vaccari, M., Tudor, T. and Vinti, G. 2019. Characteristics of leachate from landfills and dump sites in Asia, Africa and Latin America: an overview. *Waste Manage*. 95: 416-431.

(Received: 07 August 2019, Accepted: 16 September 2019)

Clay Research, Vol. 38, No. 1, pp. 35-42 (2019)

Molecular Interaction of Dextran with Urea Through Ultrasonic Technique

SUBHRARAJ PANDA*[1] AND ACHYUTA PRASAD MAHAPATRA[2]

[1]*Centurion University of Technology and Management, Odisha, India*
[2]*KBRC Degree College, Cuttack 753 011, India*

Abstract – *The study of molecular interaction using ultrasonic technique in aqueous dextran solution having concentrations range (0.10%, 0.25%, 0.50%, and 0.75% and 1%) with 6(M)urea has been carried out at four different frequencies 1MHz, 5MHz, 9MHz, 12MHz and a fixed temperature 308 K. The thermo-acoustic parameters such as Acoustic impedance (Z), Adiabatic compressibility (β), Intermolecular free length (Lf), Relaxation time (τ) and Gibb's free energy (ΔG) are evaluated from the deliberate estimations of Ultrasonic Velocity speed (U), Density (ρ) and Viscosity (η). The molecular interaction present in the liquid solution such as dipole-dipole association, hydrogen- bonding, acceptor-donor, and electrostriction is analyzed based on these parameters. These acoustic parameters are utilized to get to and clarify the nature and quality of the molecular interaction of dextran with urea.*

Key words: Dextran, Acoustic impedance (Z), Adiabatic compressibility (β), Intermolecular free length (L_F).

Introduction

The ultrasonic technique is extensively used in scientific research due to their commercial application in the field of medical science. In this, direct interaction of the ultrasonic wave with the material takes place. This plays an important role in the investigation of molecular interactions, material Characterization, physicochemically behavior, and so on. This assumes a significant job in the improvement of molecular sciences. The ultrasonic investigations are utilized to predict intermolecular interactions and estimate the thermodynamic properties of liquids solution. The ultrasonic technique in polymeric solutions is an incredible and powerful apparatus for the investigations of polymer arrangement and the behavior of polymer chain in an ultrasonic field. These studies have drawn the attention of many researchers (Ali *et al.,* 2002; Thirumaran and Jayakumar, 2009). The maximum applications of polymeric materials in different fields have necessitated investigations of the molecular interactions of polymers and solvents (Panda and Mahapatra, 2018; Panda and Mahapatra, 2018; Panda and Mahapatra, 2016; Panda and Mahapatra, 2016; Panda and Mahapatra, 2015). Utilizing the deliberate estimations of sound velocity, density, and viscosity, the thermodynamic parameters like Gibb's free energy (ΔG) as well as acoustical parameters like acoustic impedance (Z), adiabatic compressibility (β), intermolecular free length (L_F) and relaxation time (τ) etc., can be calculated.

In this paper the authors have given information regarding nature of polymer-solvent interaction and the effects of concentration on the molecular interaction of dextran in urea have been studied. In continuation of ourprior work on various concentration of solute and solvent (Panda and Mahapatra, 2018; Panda and Mahapatra, 2018; Panda and Mahapatra, 2016; Thirumaran and Jayakumar, 2009; Rajagopal, K.

***Corresponding Author Email :** subhraraj4u@gmail.com

and Chenthilnath 2010; Panda and Mahapatra, 2014), we have made a further endeavor to contemplate efficiently the physical-chemical behavior of dextran in urea. The behavior of dextran in urea has been examined with the help of ultrasonic interferometer working at constant temperature 308 K at different frequencies 1MHz, 5MHz, 9MHz, 12MHz.

A study is carried out in the aqueous solution of dextran having concentrations range (0.10%, 0.25%, 0.50%, and 0.75% and 1%) with *6(M) urea* at different frequencies (1MHz, 5MHz, 9MHz and 12MHz), ultrasonic velocity is measured and related parameters are calculated at 308K using density and viscosity. The outcomes give subjective data with respect to nature and quality of the particles interactions between solute and solvent in the liquids solutions. The chemicals used in the work have wide applications in medicine and pharmaceutical industry.

Dextran is a complex, branched polysaccharide made of numerous glucose atoms made out of chains of fluctuating length (from 10 to 150 kilodaltons). Dextran, a water-soluble polymer, is an α-D-1, 6-glucose connected glucan with side chains 1-3 connected to the backbone units of the polymer. Dextran have incredible potential for applications in different nourishment items as conditioners, stabilizers, bodying specialists or related uses. Dextran have numerous other potential applications, for example, emulsifying and thickening operators, high-consistency gums, explosives, de-flocculants in paper items, optional recuperation of oil, oil penetrating muds and soil conditioners. The existences of dextran in numerous soils and their security to impact the binding of soil particles have been noted. Extra work is accounted for managing the impact of molecular weight ranges of dextran polymers on soil molding, including information on the influence of the structural branching of dextran polymers. Checked adjustment of soils, up to 60% improved plant seedling development, and up to 70% better crop yield, have been shown with soils containing explicit dextran items.

Urea is a mineral that is only stable in an arid environment. The structure of urea the carbon is attached to oxygen by a double bond where as it is attached to two NH_2 with single bond each. Urea is utilized in numerous multi-segment strong compost details. Urea is exceptionally dissolvable in water and is in this manner likewise entirely appropriate for use in manure arrangements.

Experimental Section

Materials

The solution prepared in distilled water as a solvent for preparing the dextran solution at different concentrations. Dextran of molecular weight 70,000 utilized as a solute, is of analytical reagent grade, made by HI Media Laboratories Private Limited, India. Solvent 6(M) urea is an analytical reagent grade, made by Fisher scientific used in this state throughout the experiments.

Measurements

(a) Velocity Measurement

The speed of the ultrasonic wave in the solution has been measured utilizing an ultrasonic interferometer, working at 11 various frequency supplied by M/s Mittal Enterprises, New Delhi (Model M-84). The measuring cell of the interferometer is a specially structured twofold walled vessel with an arrangement for temperature constancy. An electronically worked advanced steady temperature shower provided by M/s Mittal Enterprises, New Delhi, (Model SSI-03spl) working in the temperature range -10 °C to 85 °C with an precision of ± 0.1K has been utilized to circulate water through the external jacket of the twofold walled estimating cell containing the test fluid.

The expression used to determine the ultrasonic velocity is

$u = 2d/T$ (m/s)

$= 2d \times \nu$

$= \lambda \times \nu$(Here-$2d=\lambda$)

Where, ν is the frequency of the generator which isused to excite the crystal; (In the present investigation, different frequency frequencies (1MHz, 5MHz, 9MHz and 12 MHz interferometer was employed) d- Separation between the reflector and crystal; T. Travel time of ultrasonic wave.

(b) Density Measurement

The densities of the solution were estimated using a 10 mL Pycnometer bottle. The Pycnometer bottle with the investigational solution was submerged in a temperature-controlled water shower. The density was estimated using the equation $\rho_2 = \frac{w_2}{w_1}\rho_1$

Where, w_1 = weight of distilled water, w_2 = Weight of investigational solution, ρ_1 = Density of water, ρ_2 = Density of investigational solution.

(c) Viscosity measurement

The viscosities of the solution were estimated using Ostwald's viscometer standardized with distilled water. The Ostwald's viscometer with the investigational solution was submerged in a temperature-controlled water shower. The time of flow was measured using an advanced stopwatch with a precision of 0.01 s. The viscosity was calculated using the equation,

$$\eta_2 = \eta_1 \left(\frac{t_2}{t_1}\right)\left(\frac{\rho_2}{\rho_1}\right)$$

Where, η_1 = Viscosity of distilled water, η_2 = Viscosity of solution, ρ_1 = Density of distilled water, ρ_2 = Density of investigational solution.

, t_1 = Time of flow of water, t_2 = Time of flow of investigational solution.

Theoretical Aspect

The data's of ultrasonic velocity, density and viscosity leads to determination of various thermo-acoustical parameters, using standard formula.

Acoustic impedance $z = u.\rho$

Adiabatic compressibility $\beta = \frac{1}{\rho u^2}$

Intermolecular free length $L_f = \frac{K_T}{u\rho^{1/2}}$

Relaxation time $\tau = \frac{4}{3}\frac{\eta}{\rho u^2}$

Gibb's free energy $\Delta G = kT \ln\frac{kT\tau}{h}$ here ρ density, U velocity, ç viscosity KT is the temperature dependent constant. KT = (93.875+0.375T) x10^{-8} 'T' is the absolute temperature; 'k' is the Boltzmann's constant and 'h' is the Planck's constant.

Results and Discussion

The experimental values of density, viscosity and speed of 6(M) urea with aqueous dextran and calculated acoustic parameters at frequencies 1MHz, 5MHz, 9MHz, 12MHz for temperature 308 K. in different concentration of dextran have been presented in Tables 1 to 4 and Figs. 1 to 12.

Urea, being a molecular substance, does not

Table 1. *Values of ρ and η of dextran solution in 6(M) urea.*

Temp. (K)	Concentration									
	0.10%		0.25%		0.50%		0.75%		1%	
	ρ kg.m^{-3}	η 10^{-3} N.s.m^{-2}	ρ kg.m^{-3}	η 10^{-3} N.s.m^{-2}	ρ kg.m^{-3}	η 10^{-3} N.s.m^{-2}	ρ kg.m^{-3}	η 10^{-3} N.s.m^{-2}	ρ kg.m^{-3}	η 10^{-3} N.s.m^{-2}
308	1075.3	0.965	1076.0	0.990	1076.8	1.036	1078.0	1.054	1079.2	1.073

Table 2. *Values of U and Z of dextran solution in 6(M) urea.*

Conc.	*U* m/s				*Z* 10^6 kg·m²/s			
	1MHz	5MHz	9MHz	12MHz	1MHz	5MHz	9MHz	12MHz
0.10%	1623.0	1616.5	1613.7	1615.0	1.745	1.738	1.735	1.737
0.25%	1624.3	1619.0	1615.5	1617.0	1.748	1.742	1.738	1.740
0.50%	1626.0	1621.0	1618.0	1619.0	1.751	1.745	1.742	1.743
0.75%	1627.5	1622.5	1619.0	1621.0	1.754	1.749	1.745	1.747
1%	1629.0	1623.0	1619.5	1621.0	1.758	1.752	1.748	1.749

Table 3. *Values of* β *and* L_f *of dextran solution in 6(M) urea.*

Conc.	β (10^{-10} m²/N)				L_F (10^{-10} m)			
	1MHz	5MHz	9MHz	12MHz	1MHz	5MHz	9MHz	12MHz
0.10%	3.531	3.559	3.571	3.566	3.761	3.776	3.782	3.779
0.25%	3.523	3.546	3.561	3.554	3.756	3.769	3.777	3.773
0.50%	3.513	3.534	3.548	3.543	3.751	3.763	3.770	3.767
0.75%	3.502	3.524	3.539	3.530	3.745	3.757	3.765	3.760
1%	3.492	3.518	3.533	3.526	3.740	3.754	3.762	3.758

Table 4. *Values of* τ *and* Δ*G of dextran solution in 6(M) urea*

Conc.	τ (10^{-13} s)				ΔG 10^{-20} kJ/mol			
	1MHz	5MHz	9MHz	12MHz	1MHz	5MHz	9MHz	12MHz
0.10%	4.542	4.578	4.594	4.587	197.56	199.05	199.69	199.39
0.25%	4.650	4.680	4.701	4.692	201.91	203.12	203.92	203.57
0.50%	4.853	4.883	4.901	4.895	209.82	210.96	211.64	211.41
0.75%	4.923	4.954	4.975	4.963	212.47	213.61	214.41	213.95
1%	4.996	5.033	5.054	5.045	215.16	216.52	217.32	216.98

dissociate into ions. These attractive forces are called intermolecular forces, which are more fragile than the covalent bonds between the atoms within the molecule. It is seen that ultrasonic velocity speed rises with rise in concentration (vol. %) of aqueous dextran in urea (Fig. 1) and furthermore acoustic impedance (Fig. 3), showing the rise in stiffness of the solution and hence association. The relationship in the constituent atoms include because of the expansion of urea prompts an opening of hydrogen bonds like that actuated by an increment in temperature this is

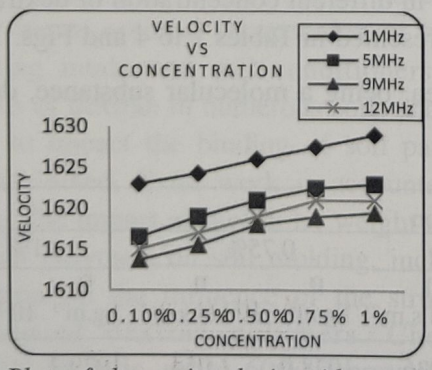

Fig. 1. *Plots of ultrasonic velocity with concentration*

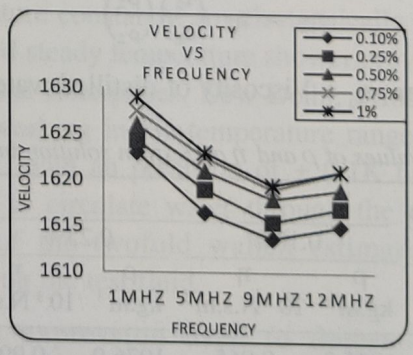

Fig. 2. *Plots of ultrasonic velocity with frequency*

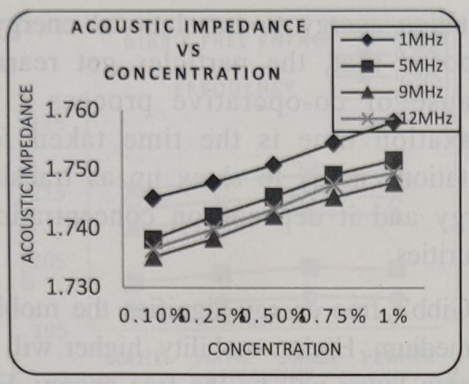

Fig. 3. *Plots of acoustic impedance with concentration*

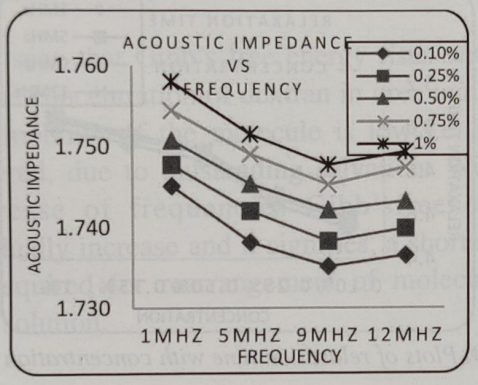

Fig. 4. *Plots of acoustic impedance with frequency*

on the grounds that the size of dextran is more than the size of water particle. Hence higher the size more will be polarizibility. So the process may lead to strong interaction forces.

The ultrasonic velocity gradually decreases with increasing frequency (Fig.2) and also acoustic impedance (Fig.4), indicating stiffness of the solutions decrease and hence dissociation but the trend is reverse at higher frequency (12MHz). This is because of the facts that, number of dextran molecules decrease and hence more polarized molecules are not available for strong interaction, means dextran molecules migrate, this behavior is typical for polymer solutions, this process leads to weak interaction force. Whereas opposite trend observed at higher frequency.

Adiabatic compressibility shows the reverse effect as compared to ultrasonic velocity. It is seen that adiabatic compressibility (β) diminishes with an expansion in the concentration of aqueous dextran in urea (Fig. 5). The rising compression of water around the dextran particles brings about a diminishing in the compressibility of solutions. The lessening in compressibility infers that there is an inclination of molecular relationship in the framework with an expansion in solute concentration. It is seen that adiabatic compressibility increments with expanding frequency (Fig. 6). When frequency increases, the interaction between the molecules in the solution changes, causing a structural change and hence an increase in adiabatic compressibility

The intermolecular free length depends on adiabatic compressibility and shows similar behavior to that of adiabatic compressibility and reverse to that of ultrasonic speed. It shows that free length decreases with increase in concentration of aqueous dextran in urea (Fig.7). This implies that breaking of polymer dextran

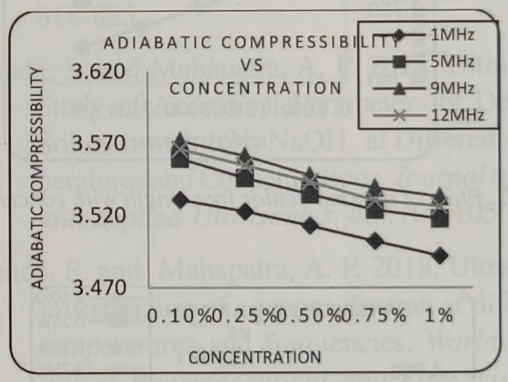

Fig 5. *Plots of adiabatic compressibility with concentration*

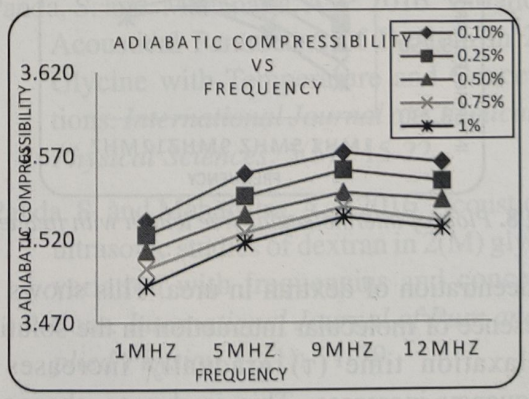

Fig 6. *Plots of adiabatic compressibility with frequency*

by mixing urea and gets associated in the structure by electrostriction in this way diminishing the free space accessible. Diminished estimation of free length shows structure advancing behavior of dextran molecule. From figure 8 as the frequency increases the intermolecular free length gradually increases indicating weak interaction among constituent molecules. This is because; number of dextran molecules decrease and more polarized molecules are not available for strong interaction. This leads to weakening of intermolecular interaction, and is reverse in case of higher frequency (12MHz).

Fig. 9 Relaxation time (τ) rises with risein

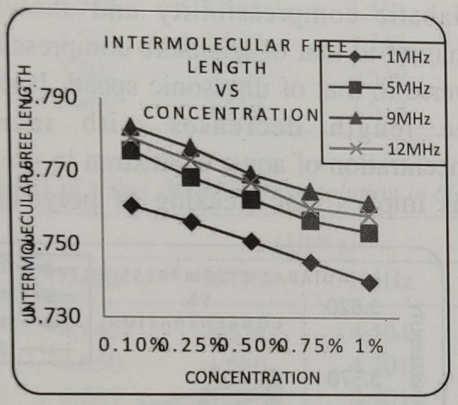

Fig 7. *Plots of intermolecular free length with concentration*

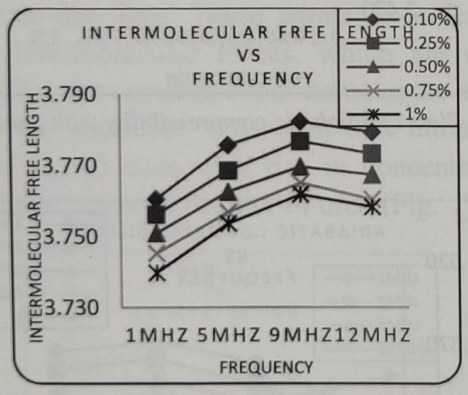

Fig 8. *Plots of intermolecular free length with frequency*

concentration of dextran in urea. This shows the presence of molecular interaction in the solution. Relaxation time (τ) gradually increases as frequency increases. This is due to change of excitation energy to translational energy. it is proposed that, the particles get rearranged because of co-operative process [19-20]. Relaxation time is the time taken for the excitation energy to show up as translational energy and it depends on concentration and impurities.

Gibb's free energy signifies the mobility of the medium. Higher mobility, higher will be the entropy; lower will be the free energy. Fig. 11.

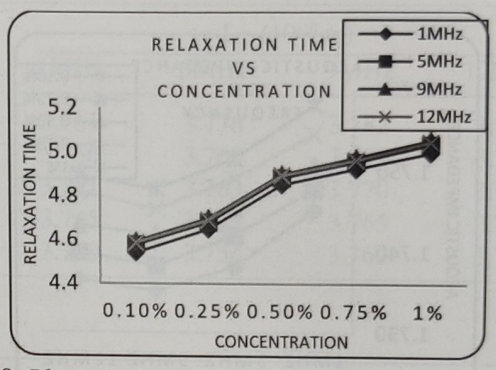

Fig. 9. *Plots of relaxation time with concentration*

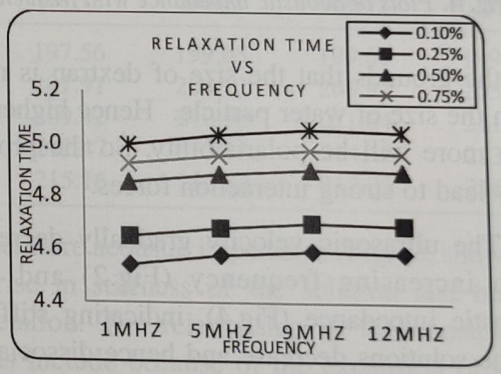

Fig. 10. *Plots of relaxation time with frequency*

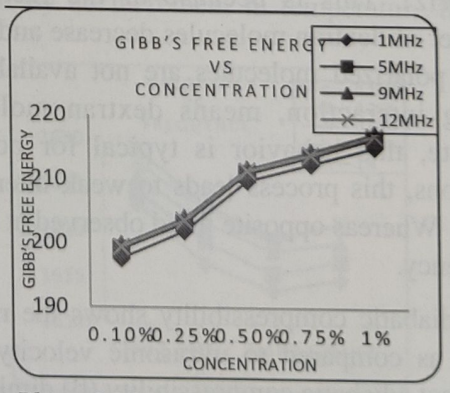

Fig. 11. *Plots of Gibb's free-energy with concentration*

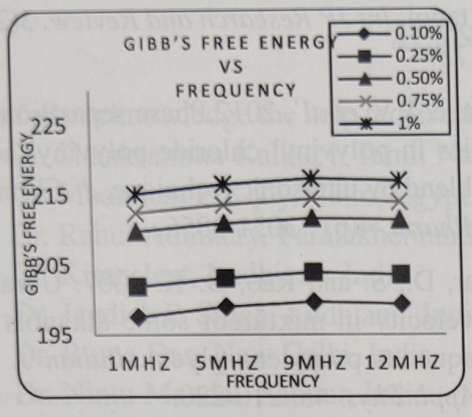

Fig. 12. *Plots of Gibb's free-energy withfrequency*

It is seen that Gibb's free energy rises with rise in the concentration of dextran in urea indicating the mobility of the molecule is low i.e. highly ordered, due to outstanding salvation. With the increase of frequencies Gibb'sfree energy gradually increase and it signifies, a shorter time is required for rearrangement of molecules in the solution.

Conclusion

Ultrasonic velocity speed, density, and viscosity have been determined experimentally for aqueous dextran solution with urea solution at various frequencies in constant temperature. By using these values various thermo acoustic parameters are calculated by using the standard formula. It is observed that ultrasonic studies provide the molecular interaction that is present between solute and solvent. This is a clear indication of intermolecular interactions because of hydrogen bonding among the solute and solvent molecules.

Acknowledgments

The principal author sincerely thanks the HOD and staff members of the Department of Physics, Centurion University of Technology and Management, Odisha, India, and ABIT management, Cuttack for their strategic help and consolation.

References

Ali, A., *et al'*.2002. Study of intermolecular interactions in binary liquid mixtures through ultrasonic speed measurements, *Ind. J. Pure and Appl. Phys.* 40: 315-322.

Thirumaran, S. and Jayakumar, J. 2009. Ultrasonic study of n-alkanols in toluene with nitrobenzene. *Ind., J. Pure and Appl. Phys.* 47: 265-272.

Rajagopal, K. and Chenthilnath, S. 2010. Molecular interaction studies and theoretical estimation ofultrasonic speeds using scaled particle theory in binary mixtures of toluene withhomologous nitriles at different temperatures. *Thermochimica Acta.* 498(1-2): 45-53.

Panda, S. and Mahapatra, A. P. 2014. Variation of thermo-acoustic parameters of dextran with concentration and temperature. *J. of Chemical and Pharmaceutical Research.* 6(10): 818-825.

Panda, S. and Mahapatra, A. P. 2018. Ultrasonic Study of Acoustical Parameters of Dextran Solution with 1(N) NaOH at Different Temperatures and Concentrations. *Journal of pure and applied Ultrasonics.* 40: 100-105.

Panda, S. and Mahapatra, A. P. 2018. Ultrasonic investigation of aqueous dextran at different temperatures and frequencies. *World Journal of Pharmaceutical and Life Sciences.* 4(12): 76-82.

Panda, S. and Mahapatra, A. P. 2016. Variation of Acoustical Parameters of Dextran in 2(M) Glycine with Temperature and Concentrations. *International Journal of Chemical and Physical Sciences.* 5(5) : 15-22.

Panda, S. and Mahapatra, A. P.2016. Acoustic and ultrasonic studies of dextran in 2(M) glycine-variation with frequencies and concentrations. *International Journal of Pure and Applied Physics.* 12(1): 71-79.

Panda, S. and Mahapatra, A. P. 2015. Study of

acoustic and thermodynamic properties of aqueous solution of dextran at different concentration and temperature through ultrasonic technique. *International Journal of Science and Research International Symposium on Ultrasonics*. 503-508.

Kawale, R.S. *et al'* 2013. Ultrasonic Behaviour of Thiophenol in Benzene, carbon tetracholoride, Cyclohexane & n-Hexane. *Bionano Frontier*. 6(2) : 204-206,

Bedare, G.R. *et al' 2012*. Studies of Acoustic and ThermodynamicProperties of Binary liquid Mixtures at 308K. *J of chem& pharmaceutical Research*. 4(2): 1028-1032.

Md. Nayeem. *et al'*. 2014. Ultrasonic Investigations of Molecular Interaction in Binary Mixtures of Benzyl Benzoate with Isomers of Butanol. *Int JP Research and Review*. 3(2): 65-78.

Tabhane, P.V. *et al'*. 2012.Phase separation studies in polyvinyl chloride-polyvinyl acetate blend by ultrasonic technique. *J. Chem. And Pharm*. 4(6) : 3051-3056.

Kumar, D., S. and Rao, D. K. 2007. Ultrasonic velocity in mixtureof some alkanols with aqueous propylene glycol. *Indian J. Pure Appl. Phys*. 45: 210-220.

Singh, D. *et al'*2014. Temperature dependent elastic and ultrasonic properties of berkelium monopnictides. *Arab. J. Sci. Eng*. 39: 485.

Ali, A. and Nain, A.K. 2002. Ultrasonic study of molecular interaction in binary liquid mixtures at 30°C. *PramanaJ. Phys*. 58(4): 695-701.

(Received: 07 August 2019, Accepted: 13 September 2019)

ACKNOWLEDGEMENT

I grate fully acknowledge the help received from the followings scientists /Professors who reviewed

1. Dr. Shankramma Kalikeri, Tamil Nadu, India
2. Dr. Moanman ElKady, Cairo, Egypt
3. Dr. Rahul Adhikary, Paralakhemundi, India
4. Dr. Kiran Jeet, Ludhiana, India
5. Dr. Jagdish P. Singh, Ludhiana, India
6. Dr. Ruma Das, New Delhi, India
7. Dr. Nintu Mandal, Sabour, India

INSTRUCTIONS FOR CONTRIBUTORS

CLAY RESEARCH is the official publication of THE CLAY MINERALS SOCIETY OF INDIA and is published twice a year, in June and December. The Journal undertakes to publish articles of interest to the international community of ceramics, civil and petroleum engineering, clay mineralogy, crystallography, geochemistry, geology, material sciences, nanotechnology, pedology, petrochemical, petrology, pharmaceutical, physical and colloid chemistry, physics, soil science, and host of other kindred academic and industrial disciplines. It does not charge authors any fees for submission, and accept papers from authors irrespective of contributing author(s) nationality, race, gender and membership of the CMSI. Its publication profile of contributing authors, editors and reviewers is international. All submitted articles undergo double-blind peer-review process and editorial scrutiny before publication.

The articles published in Clay Research are indexed in Scopus, Google Scholar, CNKI Scholar, EBSCO Discovery, and Summon (ProQuest). The Clay Minerals Society of India (CMSI) is affiliated to the Clay Minerals Society and is a member of AIPEA (Association Internationale pour I'Etude des Argiles).

Paper (in English) in MS Word (2007 or above) format should be submitted through e-mail attachment to the "Chief Editor - Clay Research" at the <cedclayres@gmail.com>. Submission is an undertaking that the manuscript has not been published or submitted for publication elsewhere.

Manuscripts should not exceed sixteen typed (double spaced) pages including tables and illustrations. Only online submission of manuscript complete in all respect is accepted.

Form: Manusciprts should be typewritten, double spaced on white paper, with wide margins with page and lines numbered. Intending contributors should consult a recent issue of CLAY RESEARCH for the standard format and style. The manuscript should have the sections ABSTRACT, introductory portion (untitled), MATERIALS AND METHODS, RESULTS and DISCUSSION and REFERENCES.

Title page should contain manuscript title, full name(s) of author(s), address (es) of the institution(s) of the author(s), a short running title not exceeding 60 characters including spaces, footnotes if any to the title, and complete mailing address of the person to whom communications should be sent.

Abstract should be a condensation of the ideas and results of the paper. It should not exceed 250 words. Do not make reference to the literature in the abstract.

Tables should have the simplest possible column headings. Type each table on a separate page; indicate location in the text by marking in the margin of text page.

Figures should be self-illustrative, drawn with black India ink on tracing paper or white Board. The lattering should be large enough to permit size reduction to one Journal page column width (about 7.0 cm) without sacrificing legibility. **The original tracing should be submitted**. The size of the drawing should not exceed 24 × 17 cm. Give the numbered legend on a separate sheet, not on the figure itself. Data available in the tables should not be duplicated in the form of illustrations. Indicate the location of the figure in the text by marking in the margin of the page.

Photographs should be in the form of glossy prints with strong contrast. In photomicrographs, the scale in micron or other suitable unit should be drawn on the print. Give the numbered legend on a separate sheet. Indicate the location of the photograph in the text by making in the margin of the text page.

References should be cited in the text by the name(s) of author(s) if two or less, and year of publication. If there are more than two authors, give the name ofthe first author followed by *'et al'* and year. Full references giving author(s) and initial(s), year, title of paper, (journal, volume, number if paged separately), first and last pages should be listed alphabetically at the end of the paper. Journal title should be abbreviated in accordance with the World List of Scientific Periodicals and its sequences. Examples are

Grim, R.E., Bray, R.H. and Bradley, W.R. 1937. The mica in argillaceous sediments. *Am. Miner.* **22**:813-829.

Brindley, G.W. 1961. Chlorite minerals. In *(G.* Brown, Ed.) *The X-ray Identification and Crystal Structures of Clay Minerals,* Mineralogical Society, London, pp.242-296.

Theng, B.K.G. 1974. *The Chemistry of Clay Organic Reactions,* Adam. Hilger, London, 343 pp.

Reprints No free reprints are supplied to authors. Order for priced reprints should be sent when required by the Editor.

Clay Research

Vol. 38 **June 2019** **No. 1**

CONTENTS

Printed at : Cambridge Printing Works, New Delhi-1100028, Cell Phone: +919811860113